

This is the author's final, peer-reviewed manuscript as accepted for publication (AAM). The version presented here may differ from the published version, or version of record, available through the publisher's website. This version does not track changes, errata, or withdrawals on the publisher's site.

# On the crystal structures and phase transitions of hydrates in the binary dimethyl sulfoxide–water system

A. D. Fortes, J. Ponsonby, O. Kirichek, V. García-Sakai

## Published version information

**Citation:** AD Fortes et al. "On the crystal structures and phase transitions of hydrates in the binary dimethyl sulfoxide–water system." *Acta Crystallographica B*, vol. 76, no. 5 (2020).

**DOI:** [10.1107/S2052520620008999](https://doi.org/10.1107/S2052520620008999)

This version is made available in accordance with publisher policies. Please cite only the published version using the reference above. This is the citation assigned by the publisher at the time of issuing the AAM. Please check the publisher's website for any updates.

1 On the crystal structures and phase transitions of hydrates in the  
2 binary system, dimethyl sulfoxide (DMSO) – water.

3

4 A. D. Fortes,<sup>1</sup> J. Ponsonby,<sup>1,2</sup> O. Kirichek,<sup>1</sup> V. García-Sakai<sup>1</sup>

5

6 <sup>1</sup>ISIS Pulsed Neutron and Muon Source, Rutherford Appleton Laboratory, Harwell Science  
7 and Innovation Campus, Chilton, Oxfordshire OX11 0QX, United Kingdom.

8 <sup>2</sup>Faculty of Science, University of Bath, Claverton Down, Bath, Somerset BA2 7AY, United  
9 Kingdom.

10

11 Corresponding author email: [dominic.fortes@stfc.ac.uk](mailto:dominic.fortes@stfc.ac.uk)

12

13

14

15

16

17 **Synopsis**

18 The crystal structures of DMSO trihydrate and DMSO dihydrate have been determined whilst  
19 a second metastable dihydrate has also been identified. The transformations between these  
20 phases, as well as their partial melting, allows us conclusively to interpret studies of the binary  
21 DMSO – water phase diagram that have been reported in the literature.

22    **Abstract**

23    Neutron powder diffraction data have been collected from a series of flash-frozen aqueous  
24    solutions of dimethyl sulfoxide (DMSO) with concentrations between 25 and 66.7 mol. %  
25    DMSO. These reveal the existence of three stoichiometric hydrates, which crystallise on  
26    warming between 175 K and 195 K. DMSO trihydrate is monoclinic, space-group  $P2_1/c$ , with  
27    unit-cell parameters at 195 K,  $a = 10.26619(3)$  Å,  $b = 7.01113(2)$  Å,  $c = 10.06897(3)$  Å,  $\beta =$   
28     $101.5030(2)^\circ$ , and  $V = 710.183(3)$  Å<sup>3</sup> ( $Z = 4$ ). Two of the symmetry inequivalent water  
29    molecules form a sheet of tiled 4- and 8-sided rings; the DMSO molecules are sandwiched  
30    between these sheets and linked along the  $b$ -axis by the third water molecule to generate water–  
31    DMSO–water tapes. Two different polymorphs of DMSO dihydrate have been identified. The  
32    alpha phase is monoclinic, space-group  $P2_1/c$ , with unit-cell parameters at 175 K,  $a =$   
33     $6.30304(4)$  Å,  $b = 9.05700(5)$  Å,  $c = 11.22013(7)$  Å,  $\beta = 105.9691(4)^\circ$ , and  $V = 615.802(4)$  Å<sup>3</sup>  
34    ( $Z = 4$ ). Its structure contains water–DMSO–water chains, but these are polymerised in such a  
35    manner as to form sheets of reniform 8-sided rings with the methyl groups extending either  
36    side of the sheet. On warming above 198 K,  $\alpha$ -DMSO·2H<sub>2</sub>O undergoes a solid-state  
37    transformation to a mixture of DMSO·3H<sub>2</sub>O + anhydrous DMSO and there is then a stable  
38    eutectic between these two phases at ~ 203 K. The beta phase of DMSO dihydrate has been  
39    observed in rapidly frozen eutectic melt and in very DMSO-rich mixtures. It is observed to be  
40    unstable with respect to the alpha phase: above ~180 K,  $\beta$ -DMSO·2H<sub>2</sub>O converts irreversibly  
41    to  $\alpha$ -DMSO·2H<sub>2</sub>O. At 175 K, the lattice parameters of  $\beta$ -DMSO·2H<sub>2</sub>O are  $a = 6.17448(10)$  Å,  
42     $b = 11.61635(16)$  Å,  $c = 8.66530(12)$  Å,  $\beta = 101.663(1)^\circ$ , and  $V = 608.684(10)$  Å<sup>3</sup> ( $Z = 4$ ),  
43    hence this polymorph is just 1.16 % denser than the alpha phase under identical conditions.  
44    Like the other two hydrates, the space-group appears likely, on the basis of systematic  
45    absences, to be  $P2_1/c$ , but the structure has not yet been determined.

46    Our results reconcile 60 years of contradictory interpretations of the phase relations in the  
47    binary DMSO – water system, particularly between mole fractions of 0.25 – 0.50, and confirm  
48    empirical and theoretical studies of the liquid structure around the eutectic composition (33.33  
49    mol. % DMSO).

50

51    **Keywords**

52    Dimethyl sulfoxide, hydrate, neutron diffraction, structure solution

53     **1. Introduction**

54     Dimethyl sulfoxide ( $[\text{CH}_3]_2\text{SO}$ , DMSO) is a well-known polar aprotic solvent with  
55 widespread applications in chemistry, biology and industry (e.g., Jacob & De La Torre, 2015:  
56 Wu & Natte, 2016: Chen & Xu, 2014), in common with the structurally similar molecules  
57 dimethyl ketone (acetone) and trimethylamine N-oxide (TMAO). Aqueous solutions of DMSO  
58 exhibit a deep melting-point depression ( $\Delta T_m \approx -70^\circ$ ) in the region of 33 mole % DMSO with  
59 a concomitant propensity to undercool and form a glass, even at low rates of cooling (Baudot  
60 *et al.*, 2000). These qualities have made the molecule useful in fields as diverse as low-  
61 temperature aqueous electrochemistry (Nian *et al.*, 2019) and the cryopreservation of biological  
62 tissues (Gurruchaga *et al.*, 2018).

63     There have therefore been numerous experimental studies of the solid-liquid equilibria  
64 (SLE) and subsolidus behaviour of the DMSO – water binary system, shown in [Figure 1](#)  
65 (Murakami & Yamada, 1962: Havemeyer, 1966: Rasmussen & MacKenzie, 1968: Rosso &  
66 Carbonnel, 1975: Khaldoyanidi *et al.*, 1983: Murthy, 1997, 1998: Mohs *et al.*, 2011: Weng *et*  
67 *al.*, 2011). The aforementioned tendency to undercool and ultimately form a glass results in a  
68 greater degree of scatter in determinations of the SLE between ~ 25 and 50 mole percent DMSO  
69 and sufficient ambiguity about the true behaviour for some striking differences of interpretation  
70 to be reported.

71     Rasmussen & MacKenzie (1968) identified a compound with a DMSO-to-water ratio of  
72 1:3 (DMSO trihydrate) which melted congruently at  $210 \pm 1$  K and exhibited a eutectic between  
73 ice and DMSO trihydrate at  $209 \pm 1$  K. On the DMSO-rich side of the system, two transitions  
74 were detected calorimetrically at 200 and 203 K. The authors inferred tentatively that there  
75 were a further two hydrates having DMSO-to-water ratios of 2:5 and 2:1, or DMSO hemi-  
76 pentahydrate and DMSO hemihydrate, respectively, both of which happened to melt  
77 incongruently at 203 K. The transition at 200 K should then be the eutectic between these two  
78 hydrates, although the authors describe it as the eutectic between the trihydrate and anhydrous  
79 DMSO.

80     Rosso and Carbonnel (1975) agreed on the existence of DMSO trihydrate, but concluded  
81 that it melted *incongruently* at 210 K. They also observed two transitions in specimens more  
82 DMSO-rich than the trihydrate, at 199 and 203 K. These were attributed to a metastable eutectic  
83 between ice and DMSO (although only observed above 30 mol. % DMSO), and a stable  
84 eutectic between DMSO trihydrate and DMSO, respectively. No other hydrates were  
85 identified.

86     Khaldoyanidi *et al.* (1983) found that DMSO trihydrate melted congruently at 210 K and  
87 identified two other hydrates, DMSO dihydrate and DMSO monohydrate. These were both  
88 reported to melt incongruently at 203 K with an additional endothermic signal at 199 K being  
89 attributed to the eutectic between the dihydrate and the monohydrate. Khaldoyanidi *et al.*  
90 (1983) noted the importance of a slow warming rate to achieving equilibrium in this system,  
91 using a rate of  $0.2 \text{ K min}^{-1}$ . These are the only authors (to date) to tabulate the temperature at  
92 which the hydrates crystallise from their amorphous precursor across a wide range of DMSO-  
93 rich compositions.

94 Lastly, Murthy (1997, 1998) carried out both calorimetric and dielectric measurements in  
95 order to both locate and better characterize the low-temperature transitions. This work agrees  
96 with Rasmussen and MacKenzie (1968) and Khaldoyanidi *et al.* (1983) in the identification of  
97 DMSO trihydrate, observing a congruent melting point at 210 K and a very shallow eutectic  
98 between ice and the trihydrate at 209 K. Again, two transitions were observed on warming of  
99 compositions more DMSO-rich than the trihydrate. Using measurements of the static dielectric  
100 constant to interpret the observations, Murthy (1997, 1998) concluded that the crystallised  
101 sample partially melted at 201 K, after which a 2–3 hr hold at 203 K led to complete  
102 recrystallization. This may be consistent with Rosso & Carbonnel’s metastable ice–DMSO  
103 eutectic model, except for the fact that their ice liquidus does not agree with any other  
104 experimental or theoretical determinations of the ice liquidus (e.g., Horsak & Slama, 1983).  
105 Murthy then detected melting at 204.5 K that, for the 1:2 composition (DMSO dihydrate), was  
106 a single-step process indicative of congruent melting. Moreover, a trihydrate–dihydrate  
107 eutectic was suggested at 203.5 K.

108 Clearly, there is some complexity to the sub-solidus behaviour at DMSO concentrations  
109 greater than 25 mol. % as well as doubt about the exact nature of the crystalline or amorphous  
110 phases that may be present. There is almost certainly a trihydrate of DMSO, and the possibility  
111 of phases with 2.5, 2.0, 1.0 and/or 0.5 water molecules for every DMSO molecule.

112 Many experimental and theoretical investigations have been made into the structure of  
113 liquid solutions of DMSO, particularly around the 1:2 composition where the melting-point  
114 depression is greatest (e.g., Soper & Luzar, 1992; Vishnyakov *et al.*, 2001; Bordallo *et al.*,  
115 2004; McLain *et al.*, 2007; Wallace *et al.*, 2015; Oh *et al.*, 2017; Stachura *et al.*, 2018; Wei *et*  
116 *al.*, 2018; Yang *et al.*, 2020). The prevailing interpretation of DMSO–water liquid data is in  
117 terms of 1:3 and 1:2 DMSO–water clusters and possible association into DMSO–(water)<sub>n</sub>–  
118 DMSO chains (Zhang *et al.*, 2009; Idrissi *et al.*, 2015; Verstakov *et al.*, 2020).

119 On the other hand, we know of only one study where diffraction-based methods were  
120 applied to study the structure of the solid phases (Boutron & Kaufmann, 1978). These authors  
121 were primarily interested in confirming the wholly amorphous nature of solids produced by  
122 rapid cooling. This was achieved by introducing liquid into a 0.2 mm gap between two Be  
123 windows and cooling it with a stream of liquid nitrogen. Transmission X-ray diffraction  
124 measurements revealed broad diffuse rings from amorphous ice and spots or Debye-Scherrer  
125 rings from single-crystals or crystalline powders of water ice. In just one of their samples,  
126 containing 45 wt. % DMSO, they noted the existence of many non-ice powder lines. The *d*-  
127 spacings of these lines are tabulated in Boutron & Kaufmann (1978) and are attributed to  
128 DMSO trihydrate but no further characterisation was reported.

129 The objectives of this work are therefore to synthesise the proposed crystalline hydrates of  
130 DMSO and to collect variable-temperature powder-diffraction data suitable for phase  
131 identification and structure solution. Neutron radiation is best suited to this work since it allows  
132 for complete structure determination, including the positions and displacement parameters of  
133 the hydrogen atoms. The solid end-member DMSO and its selenium analogue are characterised  
134 by weak C–H…O hydrogen bonds and interactions between adjacent O–S or O–Se dipoles  
135 (Ibberson 2005; Reuter, 2017; Filatov *et al.*, 2005; Gajda & Katrusiak, 2009); clearly, the  
136 hydrates must contain a mixture of both C–H…O and O–H…O hydrogen bonds and it is

137 important to make a systematic determination of how competition between these weak and  
138 medium-strength bonds, as well as other intermolecular interactions, influence the structure  
139 and properties of the various hydrates.

140

141 **2. Experimental Method**

142 **2.1 Neutron powder diffraction**

143 Five compositions were examined using neutron powder diffraction methods on the High  
144 Resolution Powder Diffractometer (HRPD) at the ISIS Neutron and Muon Spallation Source,  
145 Rutherford Appleton Laboratory, U. K. (Ibberson, 2009). Samples were prepared from  
146 perdeuterated DMSO (Sigma Aldrich 151874, 99.9 at. % D) and deuterium oxide (Sigma  
147 Aldrich 151882, 99.9 at. % D) and correspond to the numbered circles on the phase diagram in  
148 Figure 1. All five samples were in a liquid state at room temperature; after shaking to  
149 homogenise the solutions, solid specimens were prepared using a glass pipette to administer  
150 droplets directly into liquid nitrogen. Samples 1 through 4 solidified to transparent colourless  
151 spherules a few millimetres in diameter that were found to be quite brittle and hard to grind.  
152 Sample 5 solidified into opaque white spherules with a consistency similar to cream cheese,  
153 and which were consequently very easy to grind into a fine powder. Photographs of the frozen  
154 samples prior to grinding are shown in [Supplementary Figure S1](#).

155 The sample cans used for the variable-temperature high-resolution powder diffraction were  
156 the slab-geometry aluminium-alloy holders described in detail elsewhere (Fortes, 2018). As  
157 there was no shortage of sample material, all measurements were done in the largest sample  
158 cans, with internal dimensions of 18 x 23 x 15 mm. These were partially assembled and  
159 immersed in liquid nitrogen for the loading procedure. The powdered samples were transferred  
160 from a nitrogen-chilled steel cryomortar into the sample holder using a nitrogen-chilled spoon.  
161 Once filled, the ‘back’ vanadium foil window of the sample can was attached with screws.  
162 Both the ‘front’ (i.e., beam-facing) and ‘back’ windows were sealed with 1 mm indium wire to  
163 prevent leakage of material from the interior. The front windows and the body of the sample  
164 holder were masked with Gd and Cd foil.

165 The fully-assembled sample holder was then transferred into a top-loading Closed Cycle  
166 Refrigerator (CCR) mounted on the HRPD beam line at 100 K. Temperature control was  
167 achieved using a cartridge heater and a RhFe thermometer inserted into the aluminium frame  
168 of the sample holder, the background temperature of the He exchange gas being maintained  
169 ~30 K below the sample temperature where possible. Moving from one temperature to another  
170 was done at a rate of 3 K min<sup>-1</sup> (unless stated otherwise below) with a mandatory wait of 10  
171 minutes at each temperature prior to beginning a measurement in order to be sure that complete  
172 thermal equilibrium of the sample was achieved.

173 After an initial data collection at 100 K, the samples were warmed to 150 K and thereafter  
174 heated in smaller increments (10 K, reducing to 5 K and sometimes 2.5 K) in order to follow  
175 the sequence of crystallisation, transformation and melting as finely as possible in the time  
176 allowed. These measurements were comparatively short, 10 – 30 minutes. Where changes  
177 occurred slowly (for example, the crystallisation of sample 2) then data were collected in 10  
178 minute ‘snapshots’ until it was clear that the process had run its course. In other cases where it

179 was deemed necessary to acquire data with excellent statistics for an attempt at structure  
180 solution (e.g., sample 1 at 195 K), then collection times were extended to between 2 and 5 hr  
181 depending on how well the sample scattered. Samples 2, 4 and 5 were observed to be partially  
182 melted at 205 K, manifested by the disappearance of one crystalline component's Bragg peaks  
183 to leave the second crystalline component and a broad amorphous feature. Samples 2 and 4  
184 were subsequently cooled and the accessory Bragg peaks reappeared, which we interpret as  
185 recrystallization of the frozen liquid. Sample 4 was melted and re-frozen *in situ* twice.

186 Most of the data collected with the aim of tracking phase changes was done using a neutron  
187 time-of-flight window extending from 100 to 200 ms. In HRPD's backscattering detector  
188 banks, this TOF range yields data covering *d*-spacings from 2.2 to 3.9 Å. The combination of  
189 HRPD's excellent  $\Delta d/d$  resolution and the dispersion of comparatively low index Bragg peaks  
190 in this *d*-spacing range for most materials means that quite subtle changes can be followed with  
191 ease. From experience, we know that it is possible to unravel scattering from multiple unknown  
192 phases with quite 'busy' diffraction patterns using such data. Where more complete data for  
193 structure solution and refinement were needed, the timing of the instrument's incident-beam  
194 choppers was altered to use a 30–130 ms time-of-flight window. This provides access to *d*-  
195 spacings as short as 0.65 Å in backscattering, out to 10 Å in the low-resolution forward-  
196 scattering detectors.

197

## 198 **2.2 Data processing and analysis**

199 Raw time-of-flight data were focussed to a common scattering angle for each detector bank,  
200 normalised to the incident spectrum and corrected for instrument efficiency by reference to  
201 measurements of a V:Nb rod and the empty instrument with the Mantid suite of powder  
202 diffraction algorithms (Mantid, 2013; Arnold *et al.*, 2014). Stack-plots of the processed data  
203 for samples 1 – 5 are given in the Electronic Supplement ([Figures S2 – S7](#)).

204 Evaluation of all diffraction data, much of which contained contributions from several  
205 phases, allowed partitioning of Bragg peaks between four crystalline solids, one of which was  
206 anhydrous DMSO-*d*<sub>6</sub>. Peak positions from the three remaining unknowns were used to  
207 determine their diffraction indices and thus their unit-cell metrics using DICVOL06 (Louér &  
208 Boultif, 2007). Where data of suitable coverage and quality were obtained, structure solution  
209 from the power data was carried out using FOX (Favre-Nicolin & Černý, 2002, 2004). In the  
210 two instances where this was successful, the structures were fully refined by the Rietveld  
211 method in GSAS/Expgui (Larsen & Von Dreele, 2000; Toby, 2001). This also allowed for  
212 accurate phase fractions to be refined in mixtures where the structure of all constituents was  
213 known. These data are reported in [Supplementary Table S1](#).

214 Detailed analysis of the refined structures was done across a range of packages, including  
215 Diamond (Putz & Brandenburg, 2006) and Vesta (Momma & Izumi, 2011), with calculation  
216 of graph sets and searches of the Cambridge Structural Database being done with Mercury  
217 (Macrae *et al.*, 2020), and calculation of Hirschfeld surfaces and intermolecular interaction  
218 energies being done with CrystalExplorer 17.5 (Mackenzie *et al.*, 2017; Turner *et al.*, 2017).

219

220 **3. Results**

221 **3.1 Phase relations**

222 Sample-1 was initially amorphous, crystallising after warming incrementally to 195 K. The  
223 diffraction pattern obtained at this temperature was indexed as a single phase with a monoclinic  
224 unit cell of volume 710.35 Å<sup>3</sup>. Both the unit-cell volume and the bulk chemistry of the sample  
225 are consistent with a composition of DMSO-*d*<sub>6</sub>·3D<sub>2</sub>O (DMSO trihydrate) and Z = 4. Analysis  
226 of the systematic absences and a Pawley profile refinement indicated the most likely space-  
227 group to be *P*2<sub>1</sub>/c and this formed the basis for a successful structure determination. The sample  
228 was not warmed any further; instead, the fully crystallised trihydrate was cooled incrementally  
229 to 10 K in order to characterise the thermal expansion ([Suppl. Fig. S2a](#)). Some slight peak  
230 broadening occurred during cooling (see, for example, the 400 peak marked on [Suppl. Fig.](#)  
231 [S2b](#)), likely indicative of strain.

232 Sample-2 was initially amorphous but crystallised at 185 K ([Suppl. Fig. S3](#)). Unlike Sample-  
233 1, where crystallisation took a few minutes, the crystallisation of Sample-2 took approximately  
234 1 hr. The diffraction patterns were found to contain contributions from anhydrous DMSO, the  
235 newly identified DMSO trihydrate and another unknown phase. Upon warming in 5 K steps,  
236 the peaks from the unknown phase diminished in intensity and were absent at 200 K. From 200  
237 K, the two-phase mixture of DMSO + DMSO trihydrate was warmed to 205 K, where it was  
238 observed to be partially molten, leaving only peaks from the trihydrate. Cooling directly back  
239 to 175 K at 2 K min<sup>-1</sup> resulted in recrystallization of DMSO but not of the unknown phase.  
240 Peaks from the unknown phase were isolated and indexed to yield a monoclinic unit-cell of  
241 volume 617.49 Å<sup>3</sup>, indicative of the composition DMSO-*d*<sub>6</sub>·2D<sub>2</sub>O (DMSO dihydrate) and Z =  
242 4.

243 Sample-3 was initially amorphous; crystallisation occurred at 175 K over the course of ~ 1  
244 hr resulting in a diffraction pattern that contained only Bragg peaks from the phase identified  
245 in Sample-2 as DMSO dihydrate ([Suppl. Fig. S4](#)). Coupled with the bulk composition of  
246 Sample-3 (1:2) and the measurement of many more unambiguous peaks, both the indexing and  
247 phase identification were proven to be robust. Analysis of the systematic absences and a Pawley  
248 profile refinement indicated the most likely space-group to be *P*2<sub>1</sub>/c and this formed the basis  
249 for a successful determination of the dihydrate's structure. Warming in 2.5 K increments  
250 revealed that DMSO dihydrate transformed to a mixture of DMSO + DMSO trihydrate between  
251 195.0 and 197.5 K and this process was complete at 200 K.

252 Sample-4 also crystallised from an amorphous matrix at 175 K into three crystalline phases:  
253 DMSO; DMSO trihydrate; and DMSO dihydrate ([Suppl. Fig. S5](#)). The relative proportions of  
254 these remained constant up to 190 K; above that temperature, peaks from the dihydrate  
255 diminished whilst those of the other two phase grew in intensity, until the dihydrate was fully  
256 consumed somewhere between 195 and 200 K. Between 200 and 205 K the sample partially  
257 melted leaving only Bragg peaks from anhydrous DMSO.

258 This sample was then cooled at ~ 5 K min<sup>-1</sup> to 100 K, yielding a sample consisting of DMSO  
259 and an amorphous solid that we expect to have a composition close to that of the eutectic  
260 (approximately 1:2). Warming of this sample resulted in the crystallisation of a novel unknown  
261 phase at 170 K, which co-existed with DMSO dihydrate and anhydrous DMSO. At 185 K,

peaks from the unknown phase disappeared leaving only DMSO + DMSO dihydrate. As in previous samples, DMSO dihydrate gradually broke down into DMSO + DMSO trihydrate above 190 K with the process being complete at 200 K. Again, at 205 K, partial melting left only Bragg peaks from DMSO ([Suppl. Fig. S6](#)).

A second rapid cooling of Sample-4 was carried out, achieving an average rate of  $-7\text{ K min}^{-1}$  from 205 down to 100 K. However, a longer data acquisition was made on the phase mixture produced on warming to 175 K in order to better characterise the new unknown phase. After isolating unique Bragg peaks from the new phase, its powder pattern was indexed with a monoclinic unit-cell of volume  $608.64\text{ \AA}^3$ . This differs by only  $\sim 1\%$  from the volume of DMSO dihydrate suggesting the formation of a second metastable polymorph of DMSO dihydrate.

Sample-5, unlike the previous four specimens, already contained crystalline anhydrous DMSO when it was loaded at 100 K. The remaining water-bearing amorphous solid crystallised into a mixture of the  $\alpha$ - and  $\beta$ -dihydrate phases between 170 and 180 K ([Suppl. Fig. S7](#)). Above 180 K, the  $\beta$ -dihydrate was absent, and the  $\alpha$ -dihydrate began to dissociate into DMSO + DMSO trihydrate. This process of decomposition accelerated above 190 K and was complete by 200 K. The two-phase mixture of DMSO + DMSO trihydrate underwent partial melting between 200 and 205 K to leave only Bragg peaks from anhydrous DMSO.

[Figure 2](#) provides a graphical summary of the observations detailed above; quantitative data on the temperatures where amorphous-to-crystalline transitions ( $T_c$ ) were observed in this work are also annotated on [Figure 1](#). There are a number of salient points to be made about these observations. Firstly, the subsolidus transition temperatures and the observed melting points for the deuterated phases are in good agreement with the literature data obtained from protiated materials. Indeed, the calorimetric data reported recently by Ponsonby (in prep) indicates that there are no significant differences in the transition temperatures ( $T_g$ ,  $T_1$  or  $T_2$ ) between the protiated and deuterated systems; eutectic melting in the  $\text{D}_2\text{O}-\text{DMSO}-d_6$  system was observed at  $202.8 - 202.9\text{ K}$ .

It is well known that both end members of this binary system exhibit a measurable isotope effect on their melting points. The melting point of  $\text{DMSO}-h_6 = 291.67\text{ K}$  (Clever & Westrum, 1970), which increases on deuteration to  $293.7\text{ K}$  (Jakli & Van Hook, 1972; Wachter *et al.*, 2008), and hence  $\Delta T_m = +2.03\text{ K}$ . The effect is slightly larger in water, with  $\Delta T_m = +3.8^\circ$  (Kestin, 1984). Likewise, there is known to be a large isotope effect on  $T_g$  in water ice (Gainaru *et al.*, 2014; Kirichek *et al.*, 2015). However, there are many examples of systems where the effect of deuteration on transition temperatures is either smaller than expected, negligible or even negative (e.g., Miles & Menzies, 1937; Brickwedde, 1946).

Secondly, our observations on warming clearly resolve the nature of the transitions marked  $T_1$  and  $T_2$ . Transition  $T_1$  reflects the solid-state exsolution of DMSO from  $\alpha$ -DMSO dihydrate to form a composite mixture of DMSO and DMSO trihydrate. In samples of the phase-pure dihydrate, the transition is quite sharp; in compositions away from the (1:2) line, the dihydrate's dissociation is more gradual, beginning at 190 K and ending between 197.5 and 200 K. Transition  $T_2$  is simply the solidus between DMSO trihydrate and DMSO.

Thirdly, the sharp increase in  $T_c$  close to the (1:3) line agrees well with the observations made on the ice-rich side, also showing  $T_c$  rising steeply towards the trihydrate composition (Fig. 1). Khaldoyanidi *et al.* (1983) reported  $T_c$  values that are, with due consideration of the scatter, compositionally invariant (Fig. 2), which is at odds with our results. It is interesting that many physical properties of the liquid have minima or maxima corresponding with the 1:2 composition (e.g., Bordallo *et al.*, 2004; Wei *et al.*, 2018), but that the maxima we observed in  $T_c$  in the solid corresponds instead with the 1:3 composition.

310

### 311 3.2 Structures of the DMSO hydrates

#### 312 3.2.1 Structure refinement

Data collected from  $\alpha$ -DMSO dihydrate at 175 K and from DMSO trihydrate at 195 K, measured in HRPD's 30-130 ms time-of-flight window, were used for their initial structure solution. Using the FOX program, the positions of rigid DMSO and water molecules were optimized against the powder diffraction data using the parallel tempering algorithm in twenty runs of 1 million trials each. Highly reproducible structures with the best figure of merit were then transferred into GSAS for structure refinements. For both hydrates, an excellent fit of the structural model was achieved, the results of which are shown in Figure 3 for the  $\alpha$ -dihydrate and Figure 4 for the trihydrate.

A model of the  $\alpha$ -dihydrate structure with fully anisotropic atomic displacement parameters (ADPs) yielded  $wR_P = 1.29\%$  for all data and  $\chi^2 = 2.907$  for 167 variables. The refinement required inclusion of an absorption parameter and a small degree of preferred orientation (6<sup>th</sup> order spherical-harmonic model with a texture index of 1.095). Two very small regions of the diffraction pattern, marked with asterisks on Figure 3, were excluded due to the presence of artefacts from removal of the ISIS TS1 prompt pulse from the raw data.

The DMSO trihydrate model structure was similarly refined anisotropically to give  $wR_P = 1.37\%$  for all data and  $\chi^2 = 1.921$  for 221 variables. The refinement also required inclusion of an absorption parameter and a small degree of preferred orientation (8<sup>th</sup> order spherical-harmonic model with a texture index of 1.080). Two very small regions of the diffraction pattern, marked with asterisks on Figure 4, were excluded: one of these was due to the prompt pulse at 40 ms TOF and the second due to a weak parasitic Bragg peak from the vanadium windows of the CCR tail.

Table 1 reports the internal geometry of the DMSO-*d*<sub>6</sub> molecule in both hydrates compared with that found in anhydrous DMSO. Atomic coordinates, ADPs ( $U_{ij}$ ), equivalent isotropic displacement parameters ( $U_{iso}$ ) and complete tables of bond lengths and angles are provided in Supplementary CIFs. The eclipsed conformation of the methyl groups, the bond lengths and angles are common amongst sulfoxides (Calligaris, 2004). The most notable difference between the two hydrates and the anhydrous phase is the lengthening of the O–S bond with the formation of O–H…O hydrogen bonds, in agreement with Density-Functional Theory calculations. (Shun-Li *et al.*, 2010).

342

343    **3.2.2 The structure of  $\alpha$ -DMSO dihydrate**

344    The asymmetric unit of  $\alpha$ -DMSO dihydrate is shown in [Figure 5](#). Both of the symmetry-  
345    inequivalent water molecules, Ow1 and Ow2, are involved in hydrogen bonding to the oxygen  
346    atom of the DMSO molecule ([Table 2](#)). Shown in [Figure 6](#), these units are able to polymerise  
347    in such a way as to generate a 2D framework, parallel with the (001) plane, comprised of  
348    reniform 8-sided rings that are described in graph-set notation as  $R_8^6(16)$  (*cf.*, Etter *et al.*,  
349    1990). The bulky methyl groups of the DMSO molecule sit alternately above and below the  
350    ring openings. An interesting feature of this network is the trigonal pyramidal coordination of  
351    both water molecules. Although there has been some dispute in the literature (*cf.*, Liu *et al.*,  
352    2020) regarding the tetrahedral electronic structure of water (i.e., the lone-pair ‘rabbit’ or  
353    ‘squirrel’ ears) and thus an overwhelming propensity for tetrahedral coordination in ices and  
354    hydrates, it is certainly the case that trigonal coordination is quite common when the number  
355    of hydrogen-bond donors is limited.

356    The sheets of  $R_8^6(16)$  rings stack along the *c*-axis, the  $2_1$  symmetry operation causing  
357    DMSO molecules on the underside of one sheet to occupy spaces between DMSO molecules  
358    on the top of the adjacent sheet ([Figure 6](#)). Both the internal geometry and packing of the sheets  
359    is identical to that found in trimethylamine N-oxide dihydrate (CCDC code VEMFEY: Mak,  
360    1988; Enders *et al.*, 2002), although the latter crystallises in the higher-symmetry space-group  
361    *Pbca*. TMAO dihydrate manages to accommodate an extra methyl group in the interlayer space  
362    but the similarities are otherwise very clear ([Suppl. Fig. S8](#)), including the trigonal pyramidal  
363    coordination of the water molecules where there is reliable confirmatory evidence from  
364    vibrational spectroscopy (Harmon & Harmon, 1982).

365

366    **3.2.3 The structure of DMSO trihydrate**

367    The asymmetric unit of DMSO trihydrate is shown in [Figure 7](#). Two of the symmetry-  
368    inequivalent water molecules, Ow1 and Ow2, are involved in hydrogen bonding only with  
369    other water molecules ([Table 3](#)), thus forming a sheet parallel with (100) at *x* = 0.5 ([Figure 8](#)).  
370    Within this sheet, Ow1 is in trigonal coordination (donates two, accepts one H-bond) but Ow2  
371    is in a more conventional tetrahedral coordination. The water–water sheet consists of small 4-  
372    sided rings and large 8-sided rings that are described in graph-set notation as  $R_4^2(8)$  and  
373     $R_8^6(16)$  respectively ([Figure 9a](#)).

374    The third water molecule is also trigonally coordinated; it donates two hydrogen bonds  
375    solely to the sulfoxide oxygen of DMSO and accepts one H-bond from the water sheets via  
376    Ow2 ([Figure 8](#)). In this way, chains of DMSO–(water)<sub>1</sub>–DMSO molecules are generated along  
377    the *b*-axis; moreover, the DMSO molecules of adjacent indirectly-bonded chains interlock, thus  
378    forming a layer parallel with the (100) plane at *x* = 0 ([Figure 9b](#)).

379    DMSO trihydrate has no structural analogue in the CSD database (searched v. 5.41 with  
380    March 2020 update). However, there is a quite close analogue of the water–water sheet found  
381    in inorganic crystals, specifically the EDI zeolite framework, and in the structure of the high-  
382    pressure ice phase known as ice VI. [Suppl. Figure S9](#) shows the sheet of 4- and 8-sided rings  
383    that occur in the (001) plane of ice VI (Kamb, 1965) and in the silicate mineral edingtonite  
384    (Galli, 1976), the type-material for the EDI framework. Whilst there are some obvious

similarities, it is important to note that the ring nodes in ice VI and edingtonite are all tetrahedrally coordinated, so the manner in which the sheets are stacked perpendicular with (001) is quite different to DMSO trihydrate where the sheets are effectively isolated between layers of DMSO–water chains.

389

### 390 3.2.4 Comparisons between $\alpha$ -DMSO dihydrate and DMSO trihydrate

391 The O–H $\cdots$ O hydrogen-bonded frameworks of the two hydrates are evidently quite  
392 different, but we need to consider whether these are necessarily the most important structure-  
393 forming interactions (*cf.*, Gavezzotti, 2010). A comparison of the local environments of the  
394 DMSO molecules in the two structures reveals similarities and differences that appear to  
395 influence their bulk physical properties. A useful method to characterise the local interactions  
396 is by calculation of a Hirschfeld surface and derivation of two-dimensional fingerprint plots  
397 (McKinnon *et al.*, 2007; Spackman & Jayatilaka, 2009; Loon Tan *et al.*, 2019).

398 Hirschfeld surfaces for the DMSO molecules in  $\alpha$ -DMSO dihydrate and DMSO trihydrate  
399 are shown in [Figure 10](#). Red areas on the Hirshfeld surface indicate contacts that are shorter  
400 than the sum of the van der Waals radii and blue areas show where the contacts are longer than  
401 the vdW sum. The most obvious red patches on the Hirschfeld surface correspond with the O–  
402 H $\cdots$ O hydrogen bonds donated to the DMSO oxygen, but there are also some C–H $\cdots$ O contacts  
403 that fall just inside the vdW radius sum. To further understand the spectrum of longer and  
404 weaker contacts, we use fingerprint plots for both hydrates ([Fig. 11](#) and [Fig. 12](#)). These depict  
405 the distances between the Hirschfeld surface and atoms inside the surface ( $d_i$ ) against the  
406 distances to atoms outside the surface ( $d_e$ ), being further broken down into specific pairs of  
407 atomic contacts and the fractional area of the Hirschfeld surface covered by those pairwise  
408 interactions.

409 For both hydrates the O $\cdots$ H hydrogen-bonded contacts between the DMSO oxygen and  
410 water hydrogens appear as the sharply pointed region spreading to the top right from  $d_i + d_e \approx$   
411 1.793 Å. The H $\cdots$ O contacts between methyl hydrogens and both water and DMSO oxygen  
412 atoms represent a significant fraction of the Hirschfeld surface area (12–13 %). The  
413 distribution, however, has a noticeably sharper and more well-defined tip in the trihydrate than  
414 the dihydrate. There are several clear C–H $\cdots$ O hydrogen bonds in DMSO trihydrate ([Table 3](#)):  
415 C1–D1 $\cdots$ Ow3, for example, acts to stabilise the water–DMSO–water chain into what might  
416 more accurately be described as a tape ([Fig. 13](#)), and C1–D2 $\cdots$ Ow1 links the tapes back to the  
417 water–water sheets. Conversely, in the dihydrate there are fewer well-defined C–H $\cdots$ O contacts  
418 ([Table 2](#)), most of the candidate contacts being very long and/or distinctly non-linear.

419 The reason behind this difference in the C–H $\cdots$ O contacts and the striking difference in  
420 distribution of longer S $\cdots$ H and H $\cdots$ H interactions arises from the way DMSO molecules  
421 cluster in the two hydrates. Clustering occurs due to the O–S dipole-dipole interactions between  
422 DMSO molecules. These interactions may involve antiparallel (AP) dipoles or parallel dipoles  
423 ([Fig. 14](#)). Observing that the O–S–C backbone of DMSO defines a flattened trigonal pyramid,  
424 the AP interaction may occur with an edge-to-edge arrangement or a base-to-base arrangement  
425 of adjacent pyramids, both of which also allow for C–H $\cdots$ O hydrogen bonds to stabilise the  
426 dimer. Both types of antiparallel interactions and the parallel interaction occur in anhydrous

427 DMSO and represent a common mode of association in DMSO-bearing compounds. In a search  
428 of the CSD database,<sup>1</sup> edge-on AP motifs were found in 297 structures, face-to-face AP motifs  
429 in 234 structures and parallel motifs in 66 structures. Combinations are rarer, with both of the  
430 AP interactions being found together in only 43 structures.

431 In  $\alpha$ -DMSO dihydrate, close packing of DMSO molecules occurs where adjacent water–  
432 DMSO sheets interlock with those from an adjacent sheet (Fig. 15). Clearly, there is only the  
433 edge-on antiparallel type of interaction between isolated pairs of DMSO molecules.  
434 Calculation of the interaction energies in Crystal Explorer, using the B3LYP density-functional  
435 method with the 6–31G(*d,p*) basis set, shows that the total energy of the dipole-dipole  
436 interaction is  $-31.9 \text{ kJ mol}^{-1}$ , whereas the energies of the other nearest neighbour interactions  
437 are very small, or indeed positive (Fig. 15). By contrast, the interactions between DMSO  
438 dipoles in the trihydrate are more numerous and diverse. A zig-zag motif of edge-on antiparallel  
439 interactions occurs between interlocked DMSO molecules from adjacent tapes along the *b*-axis  
440 (Fig. 16). There are also parallel interactions between tapes along the *c*-axis. The geometries  
441 and interaction energies of these interactions are compared with  $\alpha$ -DMSO dihydrate and with  
442 DMSO-*d*<sub>6</sub> at 100 K (using the structure of Ibberson, 2005) in Table 4. From an electrostatic  
443 perspective, the structure of  $\alpha$ -DMSO-dihydrate might be described as a loosely bound 2D  
444 layer of DMSO dimers cross-linked by a net of water molecules. DMSO trihydrate might  
445 therefore be described as a series of more tightly-bound 3D slabs of DMSO molecules  
446 separated by sheets of ‘ice’. The paucity of dipole-dipole interactions in the dihydrate may thus  
447 explain its relative lack of stability.

448 Cyclic dimers were inferred to be present in neat liquid DMSO on the basis of infrared and  
449 Raman spectroscopic measurements (Figueroa *et al.*, 1966; Forel & Tranquille, 1970). Later  
450 authors agreed that some degree of dipole ordering was present in the liquid but considered  
451 closed cyclic dimers to be improbable (e.g., Fini & Mirone, 1976). It is nevertheless the case  
452 that closed cyclic dimers occur in anhydrous DMSO and both of the hydrates described here.  
453 Likewise, the observed propensity of DMSO to disrupt water-water hydrogen bonding in  
454 aqueous solutions, and to lower the average coordination number compared with acetone-water  
455 solutions (Bordallo *et al.*, 2004; McLain *et al.*, 2007), is preserved in the solid state as a  
456 preponderance of ‘under-saturated’ trigonally-coordinated water molecules.

457

### 458 3.2.5 A comment on $\beta$ -DMSO dihydrate

459 The so-called  $\beta$ -phase of DMSO dihydrate was observed in two separate instances, sample-  
460 4 and sample-5; in both cases, this phase crystallised from an amorphous precursor in the  
461 presence of crystalline DMSO. We hypothesis that DMSO serves as preferential nucleation  
462 agent for the  $\beta$ -dihydrate and future efforts to synthesise  $\alpha$ - and  $\beta$ -DMSO dihydrate should aim  
463 to test this possibility. Since the beta phase could not be obtained in a pure state, our indexing  
464 relies on accurate elimination of all peaks from other phases. Nevertheless, the result is  
465 extremely compelling, with high figures of merit produced by DICVOL06 [M(11) = 119.9 and

---

<sup>1</sup> Searched CSD v5.41 with March 2020 update, searching for geometric matches agreeing within 40 % in bond lengths and with 30° in bond angles. Number of structures cited excludes the seven database entries for DMSO itself.

466  $F(11) = 126.9$  (0.0018,48)] whilst also being very similar to the alpha phase in both volume  
 467 and the approximate shape (i.e., axial ratios) of the unit cell. The principal difference is that the  
 468 long axis is unique in the beta phase. A LeBail profile refinement of the best-counted dataset  
 469 containing  $\beta$ -DMSO dihydrate (Sample-4, second heating, 175 K) was done using the  
 470 tentatively assigned space-group  $P2_1/c$  (Figure 17). Since this mixture also contains  $\alpha$ -DMSO  
 471 dihydrate, it provides us with the most accurate possible determination of the difference in  
 472 molar volume between the two polymorphs, the beta phase being 1.156(2) % denser than the  
 473 alpha phase.

474

### 475 3.3 Thermal expansion of DMSO trihydrate

476 Lattice parameters of DMSO trihydrate determined between 10 and 195 K are reported in  
 477 Suppl. Table S2 and plotted explicitly in Suppl. Fig. S10. The relative change in the cell  
 478 dimensions, referenced to the values measured at 10 K, are shown in Figure 18, along with the  
 479 absolute values of the monoclinic angle,  $\beta$ , the unit-cell volume and the volume thermal  
 480 expansion coefficient. Precision at low temperatures is poorer due to strain broadening of the  
 481 Bragg peaks.

482 These data have been fitted with a second-order Grüneisen approximation to the zero-  
 483 pressure equation of state (Eq. 1). In this approximation, the thermal expansion is considered  
 484 equivalent to elastic strain such that,

$$485 V(T) = V_0 \left[ 1 + \frac{E(T)}{Q - bE(T)} \right] \quad (1)$$

486 where  $V_0$  is the unit cell volume at zero pressure,  $b = \frac{1}{2} (K'_0 - 1)$  and  $Q = (V_0 K_0 / \gamma)$ ;  $K_0$  is the  
 487 zero pressure isothermal bulk modulus,  $K'_0$  is its first derivative with respect to pressure, and  $\gamma$   
 488 is the thermal Grüneisen parameter. The internal energy due to lattice vibrations,  $E(T)$ , is then  
 489 determined via a Debye model:

$$490 E(T) = \frac{9nk_B T}{(\theta_D/T)^3} \int_0^{\theta_D/T} \frac{x^3}{e^x - 1} dx \quad (2)$$

491 where  $\theta_D$  is the Debye temperature,  $n$  is the number of atoms per formula unit, and  $k_B$  is the  
 492 Boltzmann constant; the integral term is evaluated numerically.

493 In order to be dimensionally correct, the individual lattice parameters were fitted as  $a^3$ ,  $b^3$   
 494 and  $c^3$ ; the fit parameters (along with a fit to the unit-cell volume) are given in Suppl. Table  
 495 S3. The values of  $K_0/\gamma$  reported for each axis therefore correspond with, e.g.,  $K_a/\gamma = -a^3$   
 $(dP/da^3)$ . The ‘Debye model’ fit for the  $\beta$  angle shown in Figure 18 and Suppl. Fig. S10 is  
 496 obtained simply from  $\beta = \arcsin(V / a \cdot b \cdot c)$ .

497 The Debye temperatures of between 110 and 197 K correspond to vibrational frequencies  
 498 of  $\sim 75 - 140 \text{ cm}^{-1}$ , which are typical of the low-frequency translation modes of water in ice  
 499 and hydrate crystals. The derived values of the elastic stiffness reflect the substantial anisotropy  
 500 of the crystal structure, with the unique axis having the smallest thermal expansion and being  
 least compressible. Additionally, the large derived value of  $K'$  along  $b$  indicates that the  $b$ -axis

501 stiffens quickly on compression, perhaps due to rigidity of the zig-zag motif of antiparallel O–  
502 S dipoles ([Fig. 16](#)).

503 The lattice parameters of DMSO-*d*<sub>6</sub> as a function of temperature were reported by Ibberson  
504 (2005). For comparison, the coefficient of volume thermal expansion for DMSO-*d*<sub>6</sub>·3D<sub>2</sub>O at  
505 195 K is  $\sim 2.63 \times 10^{-4} \text{ K}^{-1}$ , whilst in anhydrous DMSO-*d*<sub>6</sub> at the same temperature it is  
506  $\sim 2.42 \times 10^{-4} \text{ K}^{-1}$ . Ibberson (2005) found a Debye temperature of 252 K for the unit-cell volume  
507 of anhydrous DMSO. However, this was produced from fitting of a first-order model; when we  
508 fit a second-order model to his data (extracted graphically), we find a smaller Debye  
509 temperature,  $\theta_D \approx 171 \text{ K}$  with  $K_0/\gamma \approx 22.3 \text{ GPa}$  and  $K_0' \approx 12.2$ .

510 Whilst the relative change in axial lengths indicates that the structure is anisotropic, the true  
511 extent – and underlying origin – of the anisotropy is only apparent from a tensorial description  
512 of the thermal expansion. From this we obtain, by standard matrix decomposition methods, the  
513 eigenvalue and eigenvectors of the tensor, which are the magnitudes and the orientation of the  
514 principal expansion directions,  $\alpha_1$ ,  $\alpha_2$  and  $\alpha_3$ . For a monoclinic crystal, one direction is fixed  
515 by symmetry, so the tensor representation surface and the other two principal directions are  
516 free to adopt any orientation about the two-fold axis. The magnitudes of  $\alpha_1$ – $\alpha_3$  are plotted in  
517 [Suppl. Fig. S11](#) from both the ‘raw’ lattice-parameter data and the Debye-model fits; the  
518 temperature dependence of the volume thermal expansion coefficient,  $\alpha_V = (\alpha_1 + \alpha_2 + \alpha_3)/3$  is  
519 given in [Figure 18](#). The bulk of the structure’s thermal expansion ( $\alpha_1$ ) is approximately parallel  
520 with the (101) plane and perpendicular to *b*. The other two principal values,  $\alpha_2$  ( $\parallel b$ ) and  $\alpha_3$   
521 (orthogonal to  $\alpha_1$  and  $\alpha_2$ ) are broadly similar in value and much smaller in magnitude than  $\alpha_1$ .  
522 The small degree of negative expansion in  $\alpha_3$  below 25 K is likely an artefact of the Debye  
523 model fitting.

524 Sections of the thermal expansion tensor’s representation surface in the *a*–*c* plane, at three  
525 temperatures, are shown superimposed on the crystal structure of DMSO trihydrate in [Figure](#)  
526 [19](#). It is evident that there is no significant change in the orientation on warming and that the  
527 most obvious structural relationship is to the water–DMSO–water chains.

528

## 529 **4 Concluding remarks**

530 Crystallographic study of flash-frozen and thermally-annealed DMSO–water mixtures using  
531 neutron powder diffraction methods has identified three hydrates of DMSO, a trihydrate and  
532 two dihydrate polymorphs. We did not observe the hemipentahydrate or the hemihydrate  
533 proposed by Rasmussen and MacKenzie (1968), nor the monohydrate proposed by  
534 Khaldoyanidi *et al.* (1983) and we suggest that their inferred existence was an error of  
535 interpretation.

536 The structure of one of the dihydrate polymorphs (dubbed  $\alpha$ ) has been determined and is  
537 found to be similar to the structure of trimethylamine N-oxide dihydrate. The second ( $\beta$ )  
538 dihydrate’s structure remains unknown. The structure of the trihydrate has also been found,  
539 and this contains hydrogen-bonded structural motifs similar to those found in some zeolites.  
540 The association of DMSO into cyclic dimers as well as subunits within each crystal that may  
541 be defined as DMSO–(water)<sub>*n*</sub>–DMSO chains or sheets, agrees well with pre-existing

542 experimental and theoretical structural studies of the liquid. Dipole-dipole interactions between  
543 DMSO molecules are a major factor in the overall architecture of each structure.

544 Having determined the structure of DMSO trihydrate, we are now able to confirm that  
545 Boutron & Kaufmann (1978) probably did observe this phase in their X-ray diffraction study  
546 of nitrogen-quenched aqueous DMSO. See [Suppl. Fig. S12](#) and caption for a more detailed  
547 analysis.

548 Although we have not yet determined whether the pure trihydrate melts congruently or  
549 incongruently, we do know that the dihydrate (at least in the deuterated system at ambient  
550 pressure) is not a liquidus phase; it does not melt incongruently as proposed by Khaldoyanidi  
551 *et al.* (1983) or congruently as had been proposed by Murthy (1997, 1998). Instead, the more  
552 stable  $\alpha$ -dihydrate decomposes by solid-state exsolution to a mixture of DMSO + DMSO  
553 trihydrate at  $\sim$  198 K and this two-phase mixture then undergoes eutectic melting at 203 K. We  
554 do not detect a significant isotope effect in the temperature of these transitions.

555 The  $\beta$ -dihydrate seems only to form when anhydrous DMSO is present and we speculate  
556 that DMSO is able to preferentially nucleate the  $\beta$ -dihydrate. The  $\beta$ -dihydrate rapidly  
557 transforms to the alpha phase above  $\sim$ 180 K.

558 In order to make substantial progress with the two DMSO hydrates, it would be useful to  
559 obtain both of them phase pure, ideally as single crystals. One possible route to achieving this  
560 would be via suppression of the trihydrate, which could be realised by chemical doping or else  
561 by the application of pressure. Rasmussen and MacKenzie (1968) noted that salts appear to  
562 retard or prevent the trihydrate eutectic crystallisation. Equally, the melting point of the  
563 trihydrate may exhibit a negative or parabolic pressure dependence such that a lower hydrate  
564 is able to become the liquidus phase at high pressure; this occurs in both  $MgSO_4 \cdot 11H_2O$  and  
565  $Na_2SO_4 \cdot 10H_2O$  (Fortes *et al.*, 2013, 2017). Cansell *et al.*, (1992) examined pure DMSO and a  
566 32 mole % DMSO–water mixture (close to the dihydrate composition) up to 20 GPa in a  
567 diamond-anvil cell using Raman spectroscopy. They were able to determine that the 32 mol.  
568 % mixture froze at room temperature at 3.1 GPa. The nature of solid phase produced remains  
569 unknown and it would be interesting to determine if it is a dihydrate, a trihydrate, or some other  
570 as-yet unknown phase.

571

## 572 Acknowledgements

573 The authors thank the STFC ISIS facility for a beam time allocation, proposal RB1910287  
574 (doi:10.5286/ISIS.E.RB1910287), and the provision of technical resources with which to carry  
575 out this work. The authors also acknowledge the University of Bath science placement scheme,  
576 which allowed JP to carry out research at ISIS during 2018/19 as part of his studies in Natural  
577 Sciences.

578

## 579 References

580

581 Arnold, O., & 27 co-authors (2014) Mantid—Data analysis and visualization package for  
582 neutron scattering and  $\mu$  SR experiments. *Nucl. Instrum. Methods Phys. Res. A*, **764**, 156–  
583 166.

- 584 Baudot, A., Alger, L., & Boutron, P. (2000) Glass-forming tendency in the system water–  
585 dimethyl sulfoxide. *Cryobiol.* **40**, 151–158.
- 586 Bordallo, H. N., Herwig, K. W., Luther, B. M., & Levinger, N. E. (2004) Quasi-elastic neutron  
587 scattering study of dimethyl-sulfoxide-water mixtures: probing molecular mobility in a  
588 nonideal solution. *J. Chem. Phys.* **121**, 12457.
- 589 Boutron, P., & Kaufmann, A. (1978) Stability of the amorphous state in the system water–  
590 glycerol–dimethylsulfoxide. *Cryobiol.* **15**, 93–108.
- 591 Brickwedde, L. H. (1946) Solubility of cadmium sulfate in H<sub>2</sub>O-D<sub>2</sub>O mixtures. *J. Res. Natl.  
592 Bur. Standards* **36**(4), 377–383.
- 593 Calligaris, M. (2004) Structure and bonding in metal sulfoxide complexe: an update. *Coord.  
594 Chem. Rev.* **248**, 351–375.
- 595 Cansell, F., Fabre, D., & Petitet, J. P. (1992) Raman spectroscopy of DMSO and DMSO–  
596 H<sub>2</sub>O mixtures (32 mol % of DMSO) up to 20 GPa. *Physica B* **182**, 195–200.
- 597 Chen, S., & Xu, J. (2014) Applications of DMSO in organic semiconductor fields. *Int. J.  
598 Theoret. Phys.* **18**(4), 427–452
- 599 Clever, H. L., & Westrum Jr., E. F. (1970) Dimethyl sulfoxide and dimethyl sulfone. Heat  
600 capacities, enthalpies of fusion, and thermodynamic properties. *J. Phys. Chem.* **74**(6),  
601 1309–1317.
- 602 Enders, M., Fritz, O., & Pritzkow, H. (2002) CCDC 189203 Experimental Crystal Structure  
603 Determination. CSD Communication, doi:10.5517/cc6bwq.
- 604 Etter, M. C., MacDonald, J. C., & Bernstein, J. (1990) Graph-set analysis of hydrogen-bond  
605 patterns in organic crystals. *Acta Crystallogr. B* **46**(2), 256–262.
- 606 Favre-Nicolin, V., & Černý, R. (2002) FOX,free objects for crystallography: a modular  
607 approach to *ab initio* structure determination from powder diffraction. *J. Appl. Cryst.* **35**,  
608 734–743.
- 609 Favre-Nicolin, V., & Černý, R. (2004) A better FOX: using flexible modelling and maximum  
610 likelihood to improve direct-space *ab initio* structure determination from powder  
611 diffraction. *Z. Krist.* **219**, 847–856.
- 612 Figueroa, R. H., Roig, E., & Szmant, H. H. (1966) Infrared study on the self-association of  
613 dimethyl sulfoxide. *Spectrochim. Acta*, **22**(4), 587–592.
- 614 Filatov, A. S., Block, E., & Petrukhina, M. A. (2005) Dimethyl selenoxide. *Acta Cryst. C* **61**,  
615 o596–o598.
- 616 Fini, G., & Mirone, P. (1976) Short-range orientation effects in dipolar aprotic liquids—III.  
617 Intermolecular coupling of vibrations in sulfoxides, sulfones, nitriles and other  
618 compounds. *Spectrochim. Acta A* **32**(3), 625–629.
- 619 Forel, M. T., & Tranquille, M. (1970) Spectres de vibration du diméthylsulfoxyde et du  
620 diméthylsulfoxyde-d<sub>6</sub>. *Spectrochim. Acta A* **26**(5), 1023–1034.
- 621 Fortes, A. D., Brand, H. E. A., Vočadlo, L., Lindsay-Scott, A., Fernandez-Alonso, F., &  
622 Wood, I. G. (2013) P–V–T equation of state of synthetic mirabilite (Na<sub>2</sub>SO<sub>4</sub>·10D<sub>2</sub>O)  
623 determined by powder neutron diffraction. *J. Appl. Crystallogr.* **46**(2), 448–460.
- 624 Fortes, A. D., Fernandez-Alonso, F., Tucker, M., & Wood, I. G. (2017) Isothermal equation  
625 of state and high-pressure phase transitions of synthetic meridianite (MgSO<sub>4</sub>·11D<sub>2</sub>O)

- 626 determined by neutron powder diffraction and quasielastic neutron spectroscopy. *Acta*  
627 *Crystallogr. B* **73**(1), 33–46.
- 628 Fortes, A. D. (2018) Accurate and precise lattice parameters of H<sub>2</sub>O and D<sub>2</sub>O ice I<sub>h</sub> between  
629 1.6 and 270 K from high-resolution time-of-flight neutron powder diffraction data. *Acta*  
630 *Crystallogr. B* **74**(2), 196–216.
- 631 Gainaru, C., Agapov, A. L., Fuentes-Landete, V., Amann-Winkel, K., Nelson, H., Köster, K.  
632 W., Kolesnikov, A. I., Novikov, V. N., Richert, R., Böhmer, R. and Loerting, T. (2014)  
633 Anomalously large isotope effect in the glass transition of water. *Proc. Natl. Acad. Sci.*,  
634 **111**(49), 17402–17407.
- 635 Gajda, R., & Katrusiak, A. (2009) Electrostatic matching versus close-packing molecular  
636 arrangement in compressed dimethyl sulfoxide (DMSO) polymorphs. *J. Phys. Chem. B*  
637 **113**, 2436–2442.
- 638 Galli, E. (1976) Crystal structure refinement of edingtonite. *Acta Crystallogr. B* **32**, 1623–  
639 1627.
- 640 Gavezzotti, A. (2010) The lines-of-force landscape of interactions between molecules in  
641 crystals; cohesive *versus* tolerant and ‘collateral damage’ contact. *Acta Crystallogr. B*  
642 **66**(3), 396–406.
- 643 Gurruchaga, H., del Burgo, L. S., Hernandez, R. M., Orive, G., Selden, C., Fuller, B., Ciriza,  
644 J. & Pedraz, J. L. (2018) Advances in the slow freezing cryopreservation of  
645 microencapsulated cells. *J. Contr. Rel.* **281**, 119–138.
- 646 Harmon, K., & Harmon, J. (1982) Hydrogen bonding: Part 12. Low-temperature infrared  
647 spectra of bound water in trimethylamine N-oxide and N,N-dimethylpyrrolidinium  
648 fluoride dihydrates. *J. Mol. Struct.* **78**(1-2), 43–52.
- 649 Havemeyer, R. N. (1966) Freezing point curve of dimethyl sulfoxide–water solutions. *J.*  
650 *Pharm. Sci.* **55**(8), 851–853.
- 651 Horsak, I., & Slama, I. (1983) Calculation of the phase-diagram for the system water  
652 dimethylsulfoxide. *Coll Czech. Chem. Comm.* **48**(7), 1936–1943.
- 653 Ibberson, R. M. (2005) Neutron powder diffraction studies of dimethyl sulfoxide. *Acta Cryst.*  
654 *C* **61**, o571-o573.
- 655 Ibberson, R. M. (2009) Design and performance of the new supermirror guide on HRPD at  
656 ISIS. *Nucl. Instrum. Methods Phys. Res. A*, **600**, 47–49.
- 657 Idrissi, A., Marekha, B., Kiselev, M., & Jedlovsky, P. (2015) The local environment of the  
658 molecules in water-DMSO mixtures as seen from computer simulations and Voronoi  
659 polyhedra analysis. *Phys. Chem. Chem. Phys.* **2015**, 7, 3470–3481.
- 660 Jacob, S. W., & de la Torre, J. C. (2015) *Dimethyl Sulfoxide (DMSO) in Trauma and Disease*.  
661 CRC Press, Boca Raton.
- 662 Jakli, G., & Van Hook, W. A. (1972) The vapour pressures of dimethyl sulfoxide and  
663 hexadeuterodimethyl sulfoxide from about 313 to 453 K. *J. Chem. Thermodyn.* **4**, 857–  
664 864.
- 665 Kamb, B. (1965) Structure of ice VI. *Science* **150**, 205–209.
- 666 Kestin, J., Sengers, J. V., Kamgar-Parsi, B., & Sengers, J. L. (1984) Thermophysical  
667 properties of fluid D<sub>2</sub>O. *J. Phys. Chem. Ref. Data*, **13**(2), 601–609.

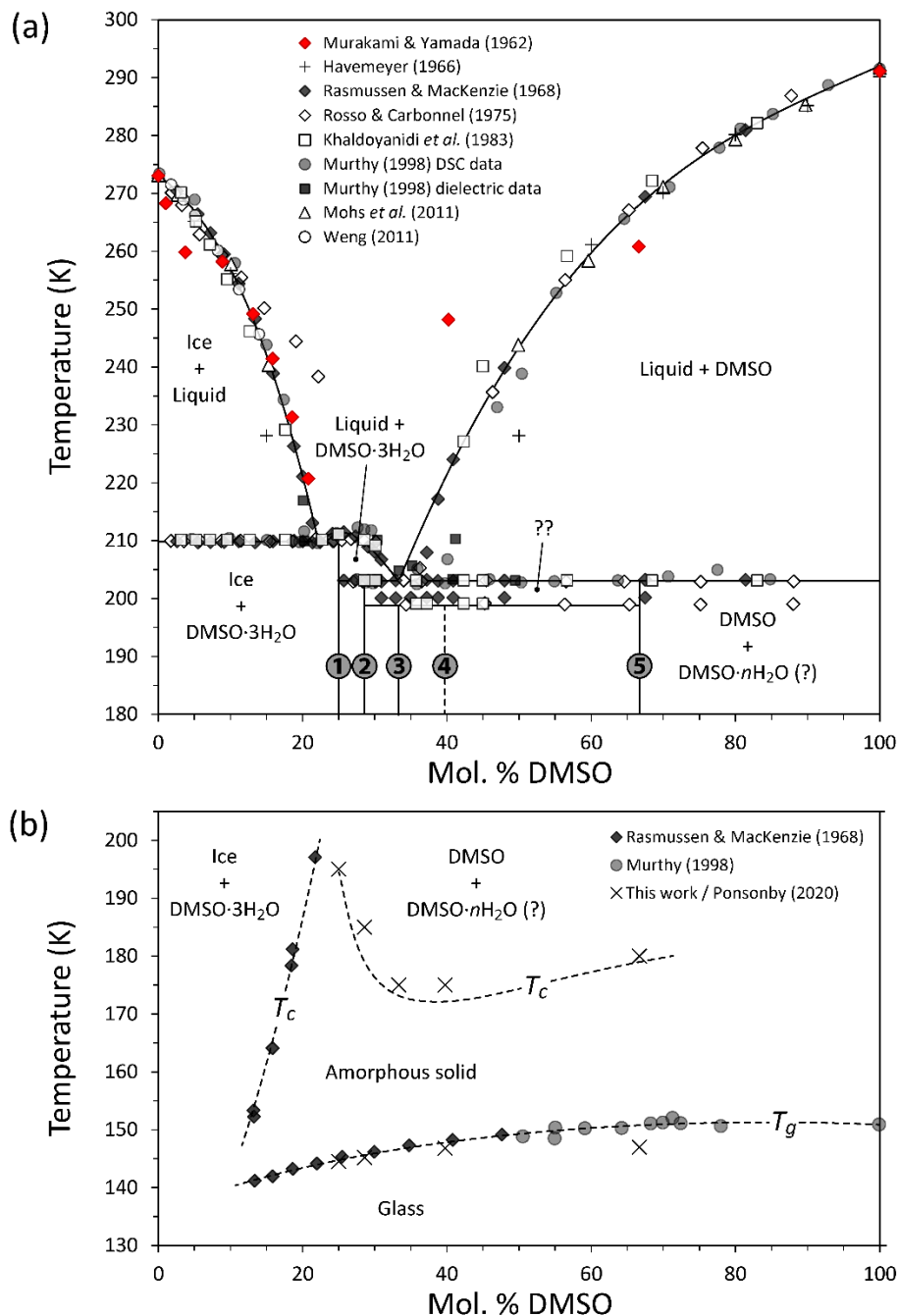
- 668 Khaldoyanidi, K. A., Grankina, Z. A., & Jacovlev, I. I. & Protasova, N. V. (1983)  
669 Исследование системы диметилсульфоксид–вода методами ДТА и ИК-  
670 спектроскопии [DTA and IR-spectroscopy investigation of the DMSO–H<sub>2</sub>O system]. *Izv.*  
671 *Sib. Otdel. Akad. Nauk SSSR. Ser. Khim. Nauk.* **1983**(2), 85–89.
- 672 Kirichek, O., Soper, A., Dzyuba, B., Callear, S., & Fuller, B. (2015) Strong isotope effects on  
673 melting dynamics and ice crystallisation processes in cryo vitrification solutions. *PloS ONE*,  
674 **10**(3), article e0120611.
- 675 Larsen, A. C. & Von Dreele, R. B. (2000). *General Structure Analysis System (GSAS)*. Los  
676 Alamos National Laboratory Report LAUR 86-748, Los Alamos, New Mexico, USA.  
677 <https://subversion.xray.aps.anl.gov/trac/EXPGUI>
- 678 Liu, Y., Frankcombe, T. J., & Schmidt, T. W. (2020) Visualizing the 30-dimensional  
679 antisymmetrized electronic structure of water: the emergence of lone pairs. *J. Phys. Chem.*  
680 *Lett.* **11**(3), 735–739.
- 681 Loon Tan, S., Jotani, M. M., & Tiekkari, E. R. T. (2019) Utilizing Hirschfeld surface  
682 calculations, non-covalent interaction (NCI) plots and calculation of interaction energies in  
683 the analysis of molecular packing. *Acta Crystallogr. E* **75**(3), 308–318.
- 684 Louër, D., & Boultif, A. (2007) Powder pattern indexing and the dichotomy algorithm. *Z.*  
685 *Kristallogr. Suppl.* **26**, 191–196.
- 686 Mackenzie, C. F., Spackman, P. R., Jayatilaka, D., & Spackman, M. A. (2017) CrystalExplorer  
687 model energies and energy frameworks: extension to metal coordination compounds,  
688 organic salts, solvates and open-shell systems. *IUCrJ* **4**(5), 575–587.
- 689 Macrae, C. F., Sovago, I., Cottrell, S. J., Galek, P. T., McCabe, P., Pidcock, E., Platings, M.,  
690 Shields, G. P., Stevens, J. S., Towler, M., & Wood, P. A. (2020). Mercury 4.0: from  
691 visualization to analysis, design and prediction. *J. Appl. Crystallogr.* **53**(1), 226–235.
- 692 Mak, T. C. W. (1988) Crystal structure of trimethylamine oxide dihydrate. *J. Mol. Struct.*  
693 **178**, 169–175.
- 694 Mantid (2013). Manipulation and Analysis Toolkit for Instrument Data; Mantid Project.  
695 <http://dx.doi.org/10.5286/SOFTWARE/MANTID>.
- 696 McKinnon, J. J., Jayatilaka, D., & Spackman, M. A. (2007) Towards quantitative analysis of  
697 intermolecular interactions with Hirschfeld surfaces. *Chem. Commun.* **2007**, 3814–3816.
- 698 McLain, S. E., Soper, A. K., & Luzar, A. (2007) Investigations on the structure of dimethyl  
699 sulfoxide and acetone aqueous solution. *J. Chem. Phys.* **127**, 174515.
- 700 Miles, F. T., & Menzies, A. W. (1937) Solubilities of cupric sulfate and strontium chloride in  
701 deuterium water. *J. Am. Chem. Soc.*, **59**(11), 2392–2395.
- 702 Mohs, A., Decker, S., & Gmehling, J. (2011) The solid-liquid equilibrium of the binary  
703 system H<sub>2</sub>O-DMSO and the influence of a salt (NaCl, KCl) on the thermodynamic  
704 behaviour. Correlations using a revised LIQUAC model. *Fluid Ph. Equilibr.* **304**, 12–20.
- 705 Momma, K., & Izumi, F. (2011) VESTA 3 for three-dimensional visualization of crystal,  
706 volumetric and morphology data. *J. Appl. Cryst.* **44**, 1272–1276.
- 707 Murakami, Y., & Yamada, T. (1962) ジメチルスルフォキシド (DMSO) – 水系の物性値  
708 [Physical properties of dimethyl sulfoxide–water system]. *Kagaku Kogaku* **26**(8), 865–  
709 872. doi:10.1252/kakoronbunshu1953.26.865.

- 710 Murthy, S. S. N. (1997) Phase behaviour of the supercooled aqueous solutions of dimethyl  
711 sulfoxide, ethylene glycol, and methanol as seen by dielectric spectroscopy. *J. Phys.*  
712 *Chem. B* **101**, 6043–6049.
- 713 Murthy, S. S. N. (1998) Some insight into the physical basis of the cryoprotective action of  
714 dimethyl sulfoxide and ethylene glycol. *Cryobiol.* **36**, 84–96.
- 715 Nian, Q., Wang, J., Liu, S., Sun, T., Zheng, S., Zhang, Y., Tao, Z., & Chen, J. (2019)  
716 Aqueous batteries operated at –50 °C. *Angew. Chem.* **131**, 17150–17155.
- 717 Oh, K. I., Rajesh, K., Stanton, J. F., & Baiz, C. R. (2017) Quantifying hydrogen–bond  
718 populations in dimethyl sulfoxide/water mixtures. *Angew. Chem. Int. Ed.* **129**, 11533–  
719 11537.
- 720 Ponsonby, J. (in preparation) *In-situ* calorimetry with quasi-elastic neutron spectroscopy:  
721 Reaslising a complementary dynamic and thermodynamic sample description. *ISIS*  
722 *Technical Report*.
- 723 Putz, H., & Brandenburg, K. (2006) *Diamond - Crystal and Molecular Structure*  
724 *Visualization*. Crystal Impact - GbR, Kreuzherrenstr. 102, 53227 Bonn, Germany.  
725 (<http://www.crystalimpact.com/diamond>)
- 726 Rasmussen, D. H., & MacKenzie, A. P. (1968) Phase diagram for the system water–  
727 dimethylsulphoxide. *Nature*, **220**, 1315–1317.
- 728 Reuter, H. (2017) Structural parameters of dimethyl sulfoxide, DMSO, at 100 K, based on a  
729 redetermination by use of high-quality single-crystal X-ray data. *Acta Crystallogr. E* **73**,  
730 1405–1408.
- 731 Rosso, J.-C., & Carbonnel, L. (1975) Le système binaire eau–diméthylsulfoxyde. *C. R. Acad.*  
732 *Sci. Paris., Série C*, **281**, 955–958.
- 733 Shun-Li, O., Nan-Nan, W., Jing-Yao, L., Cheng-Lin, S., Zuo-Wei, L., Shu-Qin, G. (2010)  
734 Investigation of hydrogen bonding in neat dimethyl sulfoxide and binary mixture (dimethyl  
735 sulfoxide + water) by concentration-dependent Raman study and *ab initio* calculation. *Chin.*  
736 *Phys. B* **19**(12), article 123101.
- 737 Soper, A. K., & Luzar, A. (1992) A neutron diffraction study of dimethyl sulphoxide–water  
738 mixtures. *J. Chem. Phys.* **97**, 1320–1331.
- 739 Spackman, M. A., & Jayatilaka, D. (2009) Hirschfeld surface analysis. *CrystEngComm*,  
740 **2009**(11), 19–32.
- 741 Stachura, S. S., Malajczuk, C. J., & Mancera, R. L. (2018) Molecular dynamics simulations of  
742 a DMSO/water mixture using the AMBER force field. *J. Mol. Mod.* **24**, article 174.
- 743 Toby, B. H. (2001) EXPGUI, a graphical user interface for GSAS. *J. Appl. Cryst.* **34**, 210–213.
- 744 Turner, M. J., McKinnon, J. J., Wolff, S. K., Grimwood, D. J., Spackman, P. R., Jayatilaka, D.  
745 & Spackman, M. A. (2017). *CrystalExplorer17*. University of Western Australia.  
746 (<http://hirshfeldsurface.net>)
- 747 Verstakov, E. S., Korobkova, S. A., & Nosaeva, T. A. (2020) Structure of dimethylsulfoxide  
748 water solutions, according to static inductivity data. *Russ. J. Phys. Chem. A* **94**, 738–741.
- 749 Vishnyakov, A., Lyubartsev, A. P., & Laaksonen, A. (2001) Molecular dynamics simulations  
750 of dimethyl sulfoxide and dimethyl sulfoxide–water mixture. *J. Phys. Chem. A* **105**, 1702–  
751 1710.

- 752 Wachter, P., Schweiger, H.-G., Wudy, F., & Gores, H. J. (2008) Efficient determination of  
753 crystallisation and melting points at low cooling and heating rates with novel computer  
754 controlled equipment. *J. Chem. Thermodyn.* **40**, 1542–1547.
- 755 Wallace, V. M., Dhumal, N. R., Zehentbauer, F. M., Kim, H. J., & Kiefer, J. (2015) Revisiting  
756 the aqueous solutions of dimethyl sulfoxide by spectroscopy in the mid-and near-infrared:  
757 Experiments and Car–Parrinello simulations. *J. Phys. Chem. B* **119**, 14780–14789.
- 758 Wei, Q., Zhou, D., Li, X., Chen, Y., & Bian, H. (2018) Structural dynamics of dimethyl  
759 sulfoxide aqueous solutions investigated by ultrafast spectroscopy: using thiocyanate  
760 anion as a local vibrational probe. *J. Phys. Chem. B* **121**, 12131–12138.
- 761 Weng, L., Li, W., Zuo, J., & Chen. C. (2011) Osmolality and unfrozen water content of aqueous  
762 solutions of dimethyl sulfoxide. *J. Chem. Eng. Data* **56**, 3175–3182.
- 763 Wu, X. F., & Natte, K. (2016) The applications of dimethyl sulfoxide as reagent in organic  
764 synthesis. *Adv. Synth. Cat.* **358**(3), 336–352.
- 765 Yang, B., Cao, X., Wang, C., Wang, S. & Sun, C. (2020) Investigation of hydrogen bonding  
766 in water/DMSO binary mixtures by Raman spectroscopy. *Spectrochim. Acta A* **228**, article  
767 117704.
- 768 Zhang, Q., Zhang, X., & Zhao, D.-X. (2009) Polarizable force field for water-dimethyl  
769 sulfoxide systems: II properties of mixtures by molecular dynamics simulations. *J. Mol. Liq.*  
770 **145**(2), 67–81.

771 **Figures and captions**

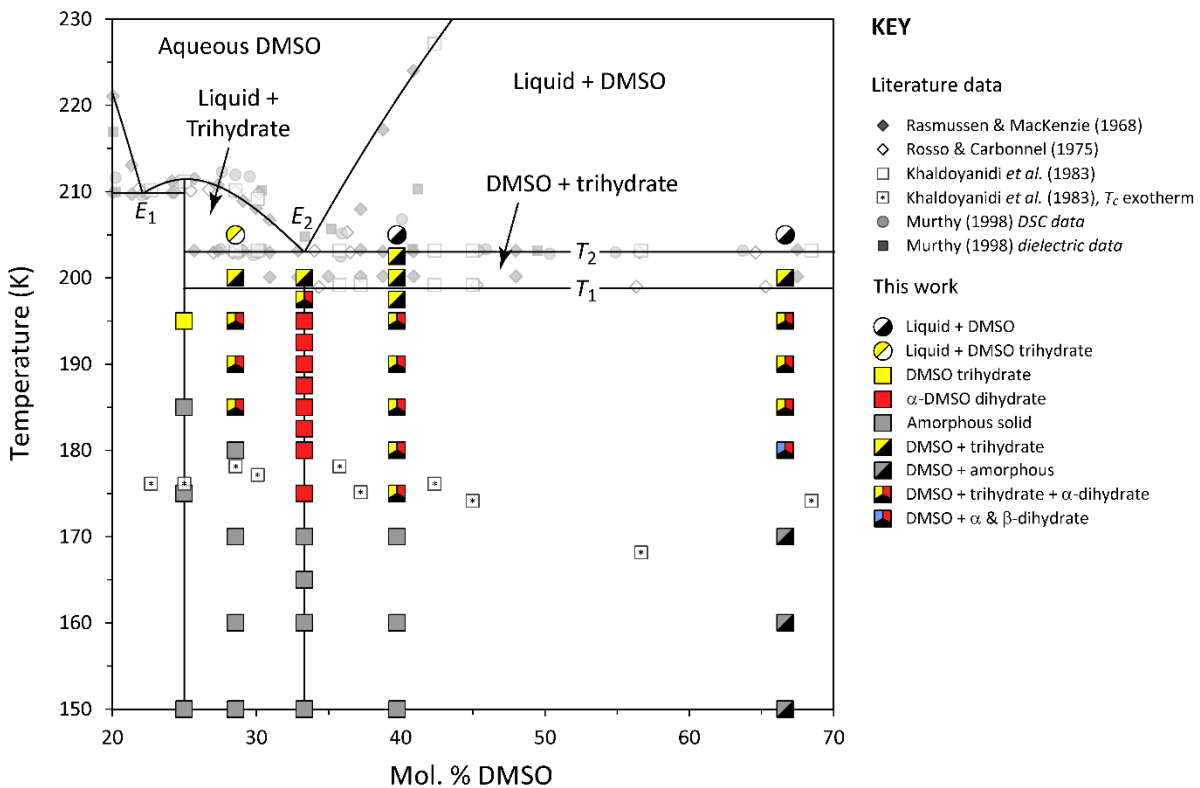
772



773

774 **Figure 1**

775 The binary phase diagram water-DMSO; symbols report literature data, mostly extracted from  
 776 published figures by graphical methods, showing solid-liquid equilibria and some sub-solidus  
 777 transitions. Panel (b) underneath isolates the glass transition ( $T_g$ ) and the crystallisation  
 778 temperature of the amorphous solid ( $T_c$ ). The vertical numbered lines indicate the compositions  
 779 of the samples used in our study. Other curved and straight lines are our own polynomial fits  
 780 to the ice and DMSO liquidus curves and reflect our interpretation of the solid-solid and solid-  
 781 liquid transitions. An expanded view of the diagram's central region is shown in Figure 2.

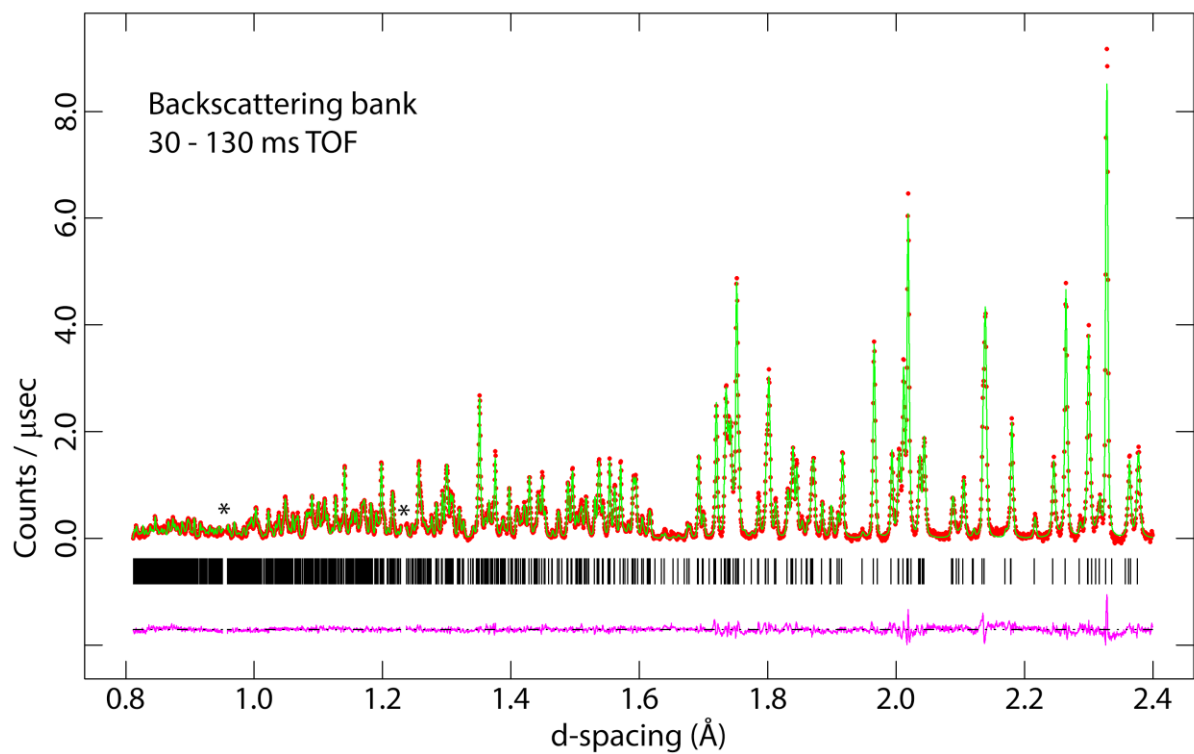


782

783 **Figure 2**

784 Expanded central region of the water–DMSO binary phase diagram. Large coloured symbols  
 785 show the loci of data acquired from samples 1 to 5 at various temperatures. Other faint symbols  
 786 report literature data from Figure 1. The vertical lines denote the composition of the  
 787 stoichiometric trihydrate and dihydrate. The horizontal line labelled  $T_1$  is the solid-state  
 788 reaction  $\alpha$ -DMSO dihydrate  $\rightarrow$  DMSO + DMSO trihydrate, and  $T_2$  is the eutectic melting point  
 789 of the DMSO / DMSO trihydrate mixture ( $E_2$  being the estimated composition of the eutectic).  
 790  $E_1$  is the location of the ice – DMSO trihydrate eutectic.

791



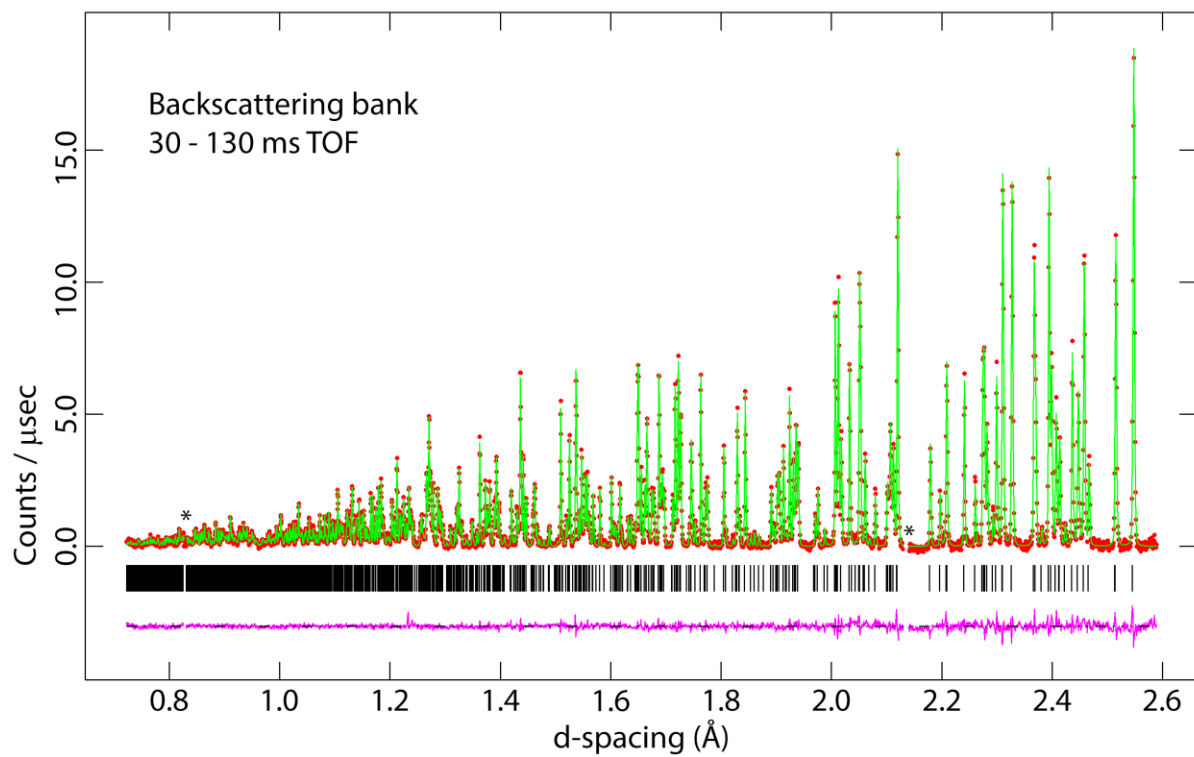
792

793

794 **Figure 3**

795 Neutron powder diffraction pattern of  $\alpha$ -DMSO dihydrate measured on HRPD at 175 K, with  
796 the background subtracted. Red circles mark the observations, the green line is the fitted  
797 structural model and the purple line underneath is the difference between the observations and  
798 the model. Vertical black tick marks show the expected positions of Bragg reflections.  
799 Asterisks mark two small excluded regions.

800



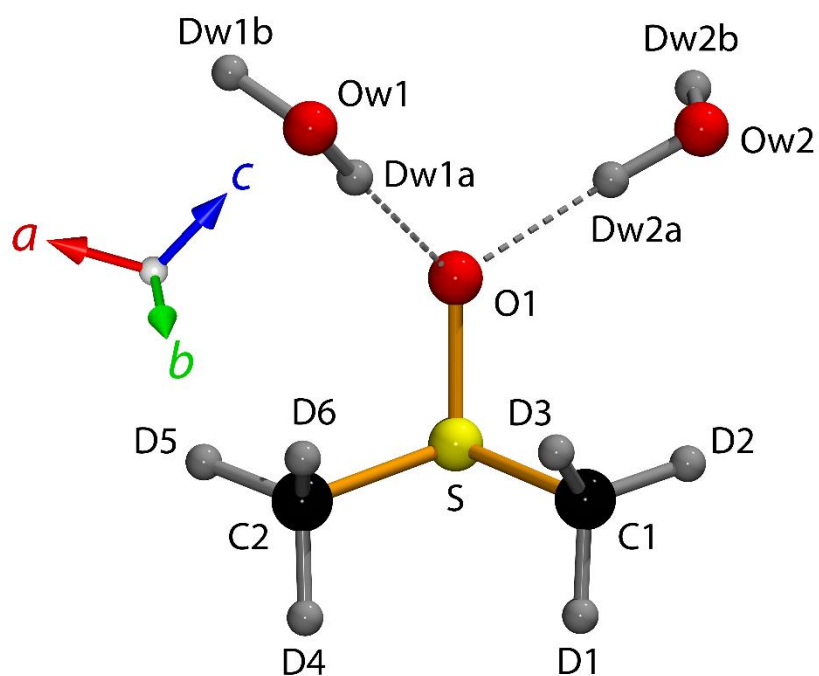
801

802

**Figure 4**

804 Neutron powder diffraction pattern of DMSO trihydrate measured on HRPD at 195 K, with the  
 805 background subtracted. Red circles mark the observations, the green line is the fitted structural  
 806 model and the purple line underneath is the difference between the observations and the model.  
 807 Vertical black tick marks show the expected positions of Bragg reflections. Asterisks mark two  
 808 small excluded regions.

809



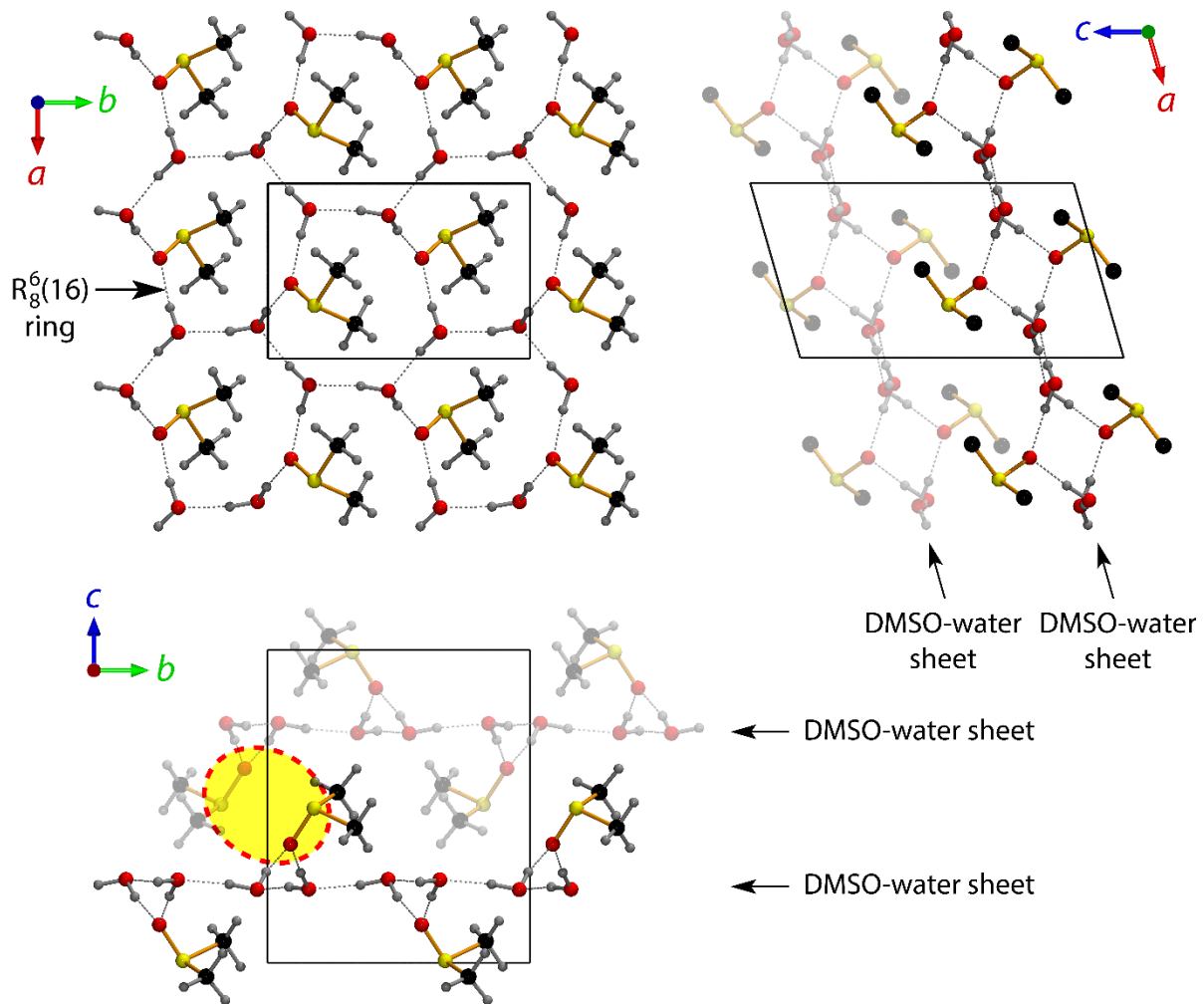
810

811

812 **Figure 5**

813 Asymmetric unit of  $\alpha$ -DMSO dihydrate; dashed rods denote hydrogen bonds.

814



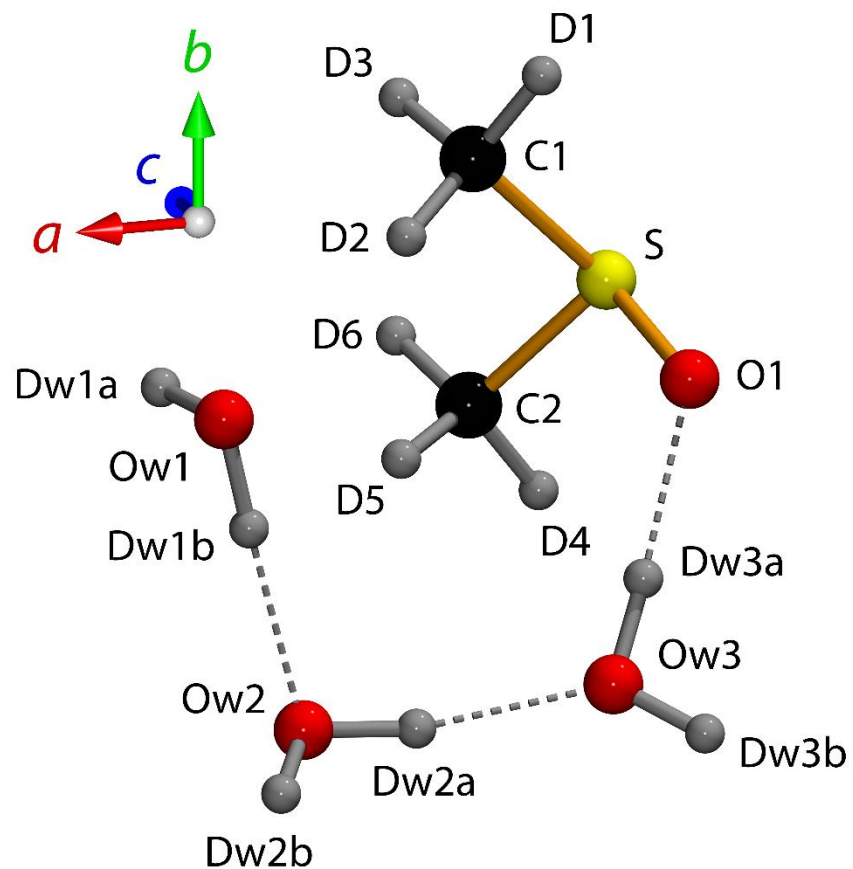
815

816

817 **Figure 6**

818 Molecular connectivity and packing in  $\alpha$ -DMSO dihydrate. The view at top left down the  $c$ -  
 819 axis shows the tiling of  $R_g^6(16)$  rings to form sheets parallel with (001). Views along the  $b$ -axis  
 820 (top right) and along the  $a$ -axis (bottom left) show the stacking of the sheets and resulting  
 821 packing of DMSO molecules from adjacent sheets, which brings antiparallel O–S dipole pairs  
 822 into proximity (red-dashed oval). Methyl hydrogens have been omitted from the illustration at  
 823 top right for clarity. Solid black lines show the unit-cell edges.

824



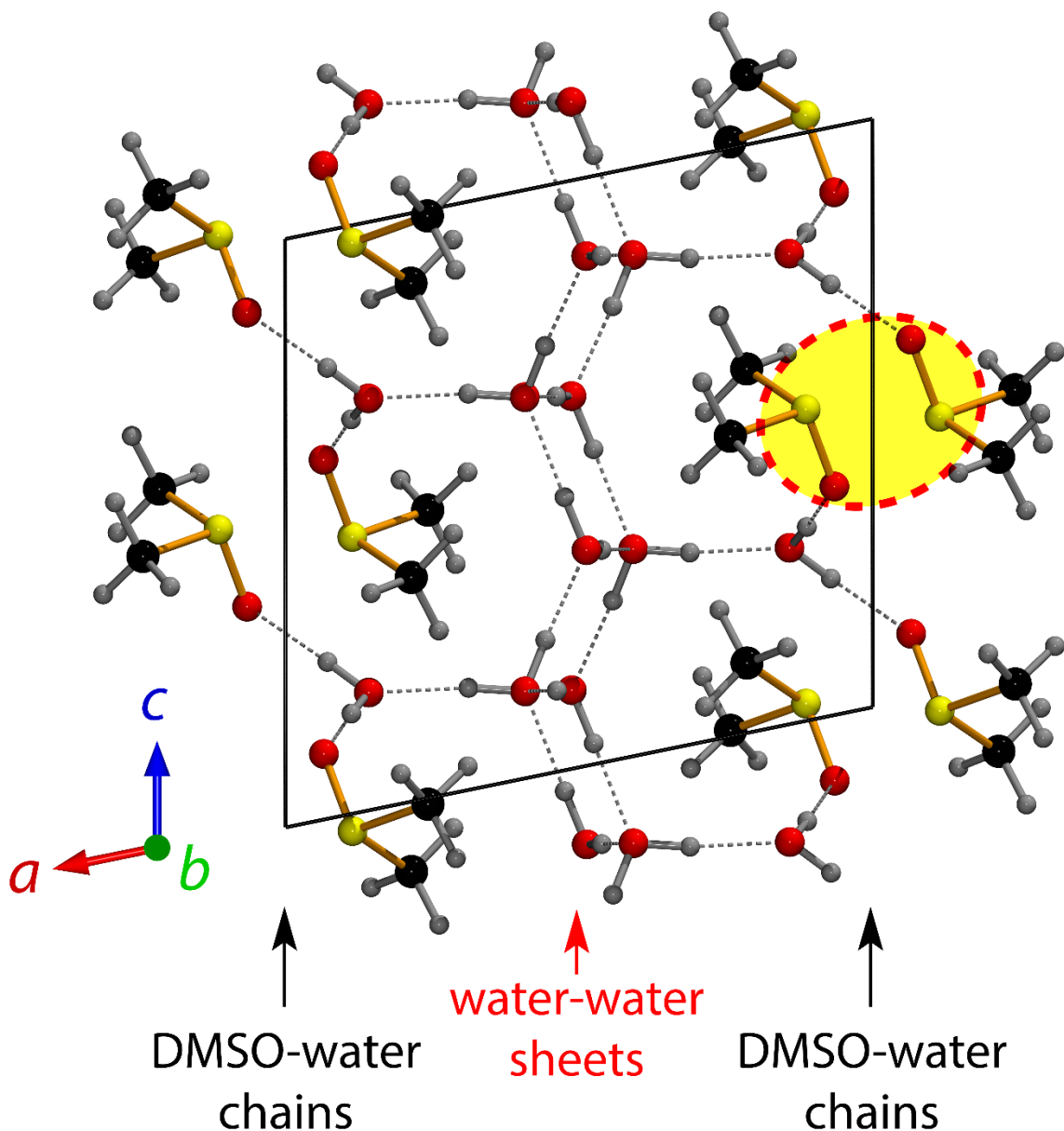
825

826

827 **Figure 7**

828 Asymmetric unit of DMSO trihydrate; dashed rods denote hydrogen bonds.

829



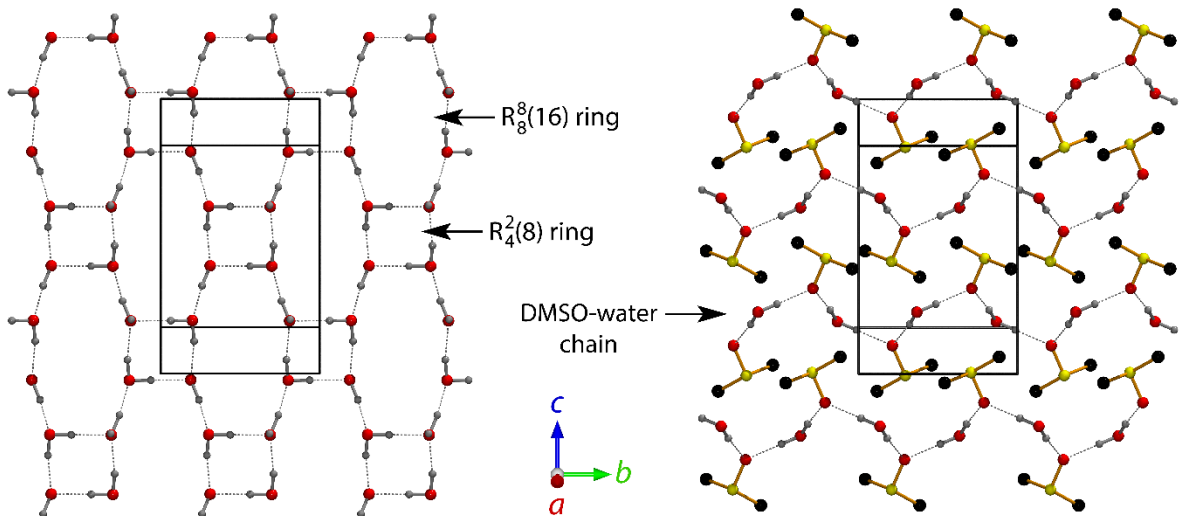
830

831

832 **Figure 8**

833 Molecular connectivity and packing in DMSO trihydrate projected along the *b*-axis. The  
 834 configuration of the water–water sheets and the DMSO–water chains perpendicular to the plane  
 835 of this figure is shown in Figure 9. The interlocking of DMSO molecules from adjacent chains  
 836 along the *b*-axis brings antiparallel O–S dipole pairs into proximity (red-dashed oval). Solid  
 837 black lines show the unit-cell edges.

838



839

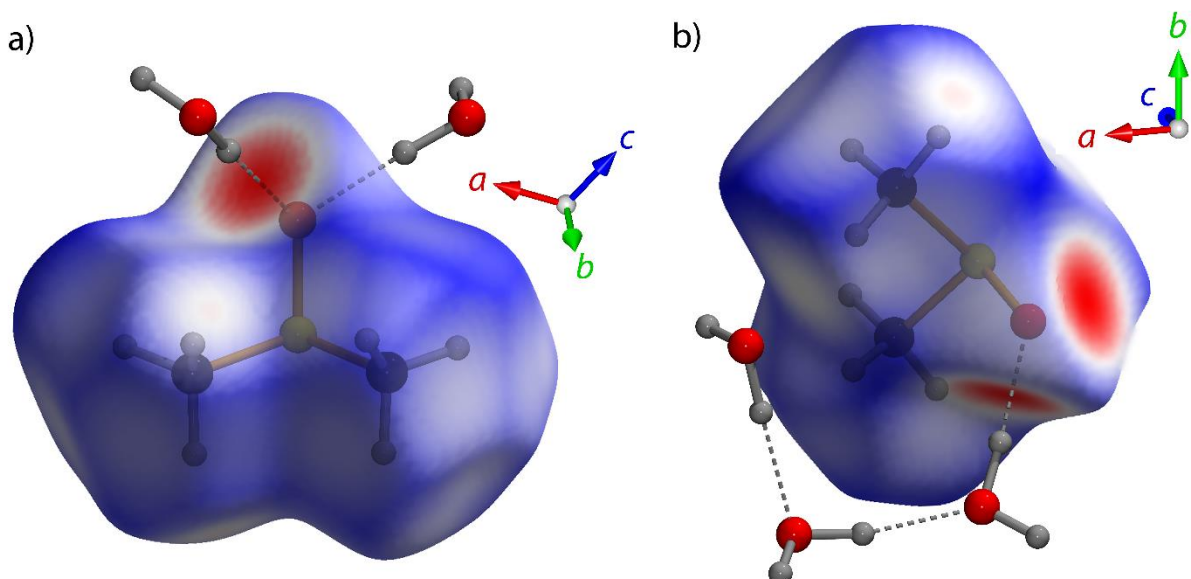
840

**841 Figure 9**

842 The configuration of the water–water sheets (left) and the DMSO–water chains (right) in  
 843 DMSO trihydrate projected along  $a^*$ . Methyl hydrogens have been omitted from the illustration  
 844 on the right for clarity. Solid black lines show the unit-cell edges.

845

846



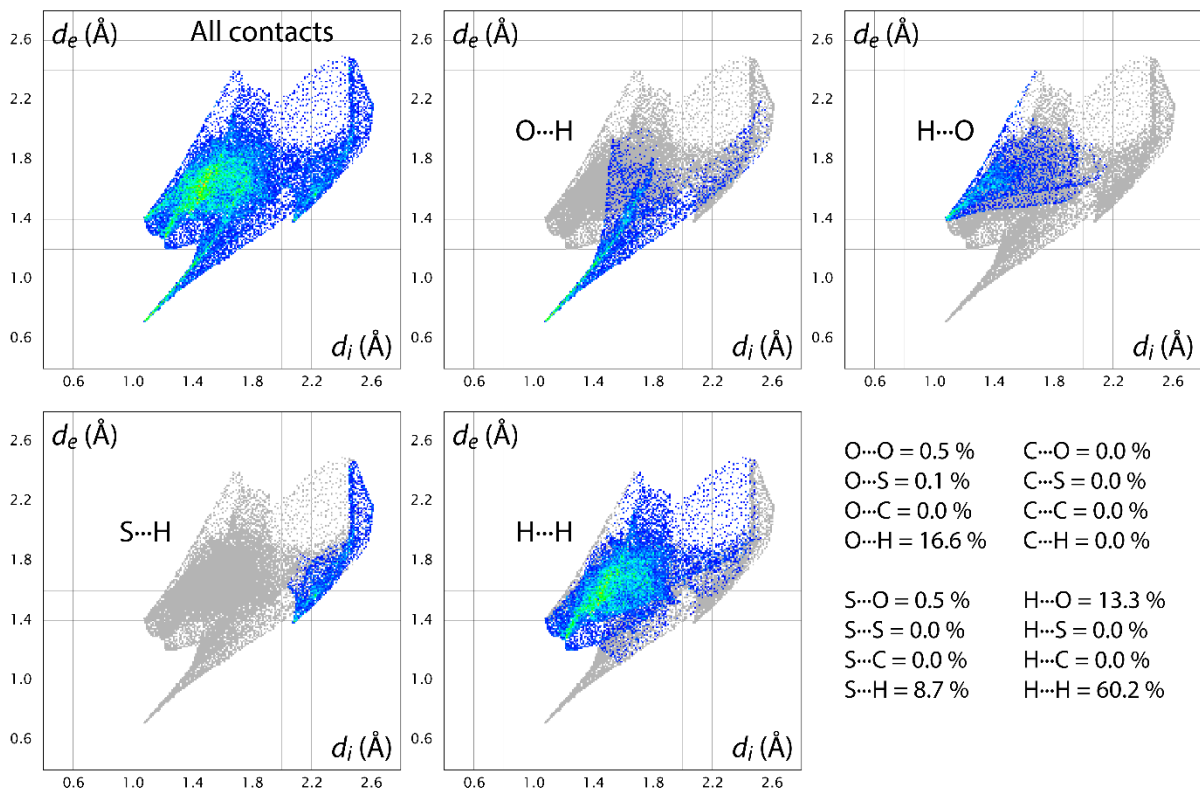
847

848

849 **Figure 10**

850 Hirschfeld surfaces of the DMSO molecules in  $\alpha$ -DMSO dihydrate (left)  
851 and DMSO trihydrate (right) superimposed over the asymmetric units shown in  
852 Figures 5 and 7. For the dihydrate, the  $d_{norm}$  values range from -0.6477 (red) to 1.1648 (blue)  
853 and the enclosed volume is 102.22  $\text{\AA}^3$ . For the trihydrate, the  $d_{norm}$  values range from -0.6680 (red) to 1.1537 (blue)  
854 and the enclosed volume is 99.96  $\text{\AA}^3$

855



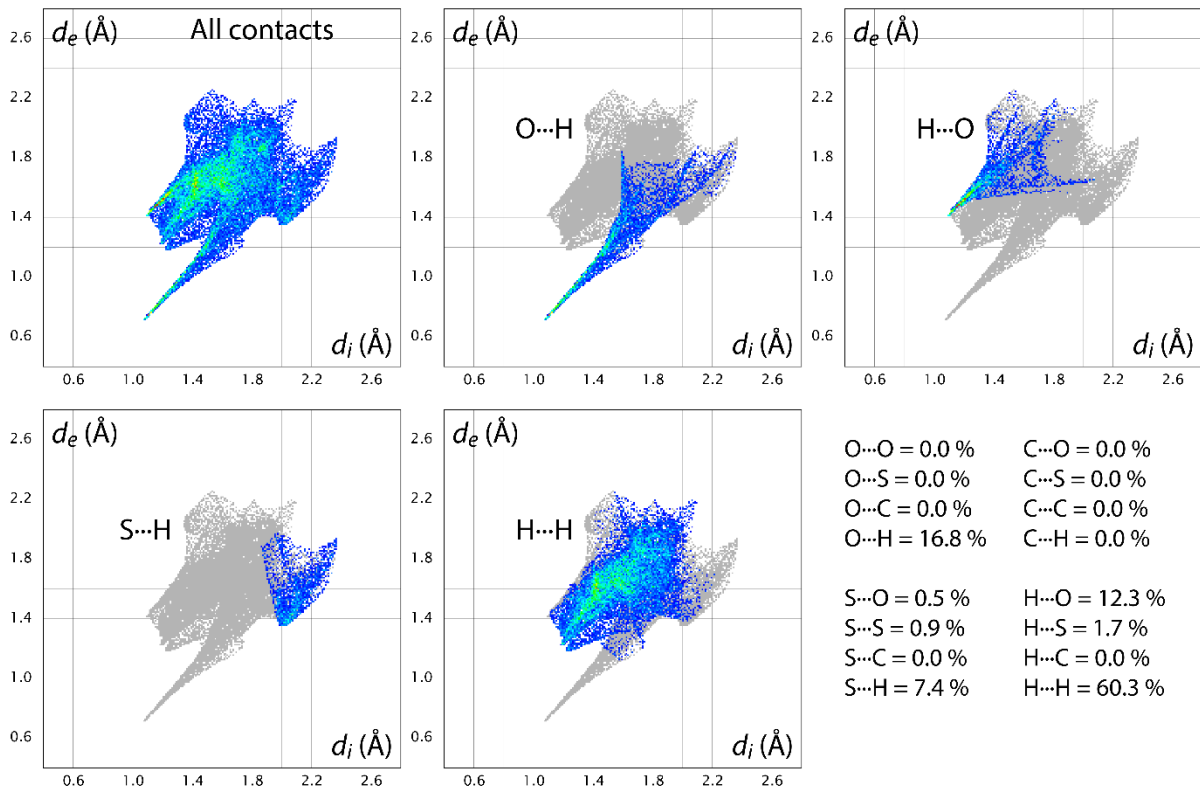
856

857

858 **Figure 11**

859 Fingerprint plots for the DMSO molecule in  $\alpha$ -DMSO dihydrate. The fractional area of the  
 860 Hirschfeld surface for any given set of pairwise interactions is listed at bottom right.

861



$O\cdots O = 0.0 \%$	$C\cdots O = 0.0 \%$
$O\cdots S = 0.0 \%$	$C\cdots S = 0.0 \%$
$O\cdots C = 0.0 \%$	$C\cdots C = 0.0 \%$
$O\cdots H = 16.8 \%$	$C\cdots H = 0.0 \%$
$S\cdots O = 0.5 \%$	$H\cdots O = 12.3 \%$
$S\cdots S = 0.9 \%$	$H\cdots S = 1.7 \%$
$S\cdots C = 0.0 \%$	$H\cdots C = 0.0 \%$
$S\cdots H = 7.4 \%$	$H\cdots H = 60.3 \%$

862

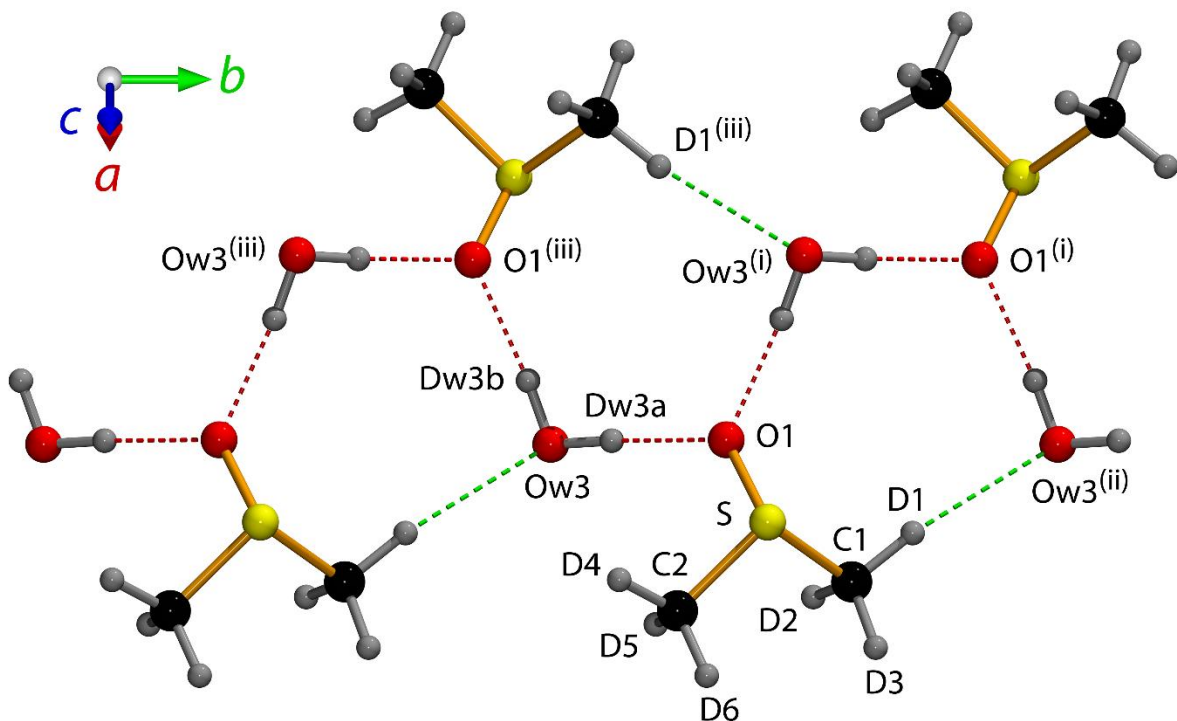
863

### 864 **Figure 12**

865 Fingerprint plots for the DMSO molecule in DMSO trihydrate. The fractional area of the  
 866 Hirschfeld surface for any given set of pairwise interactions is listed at bottom right.

867

868



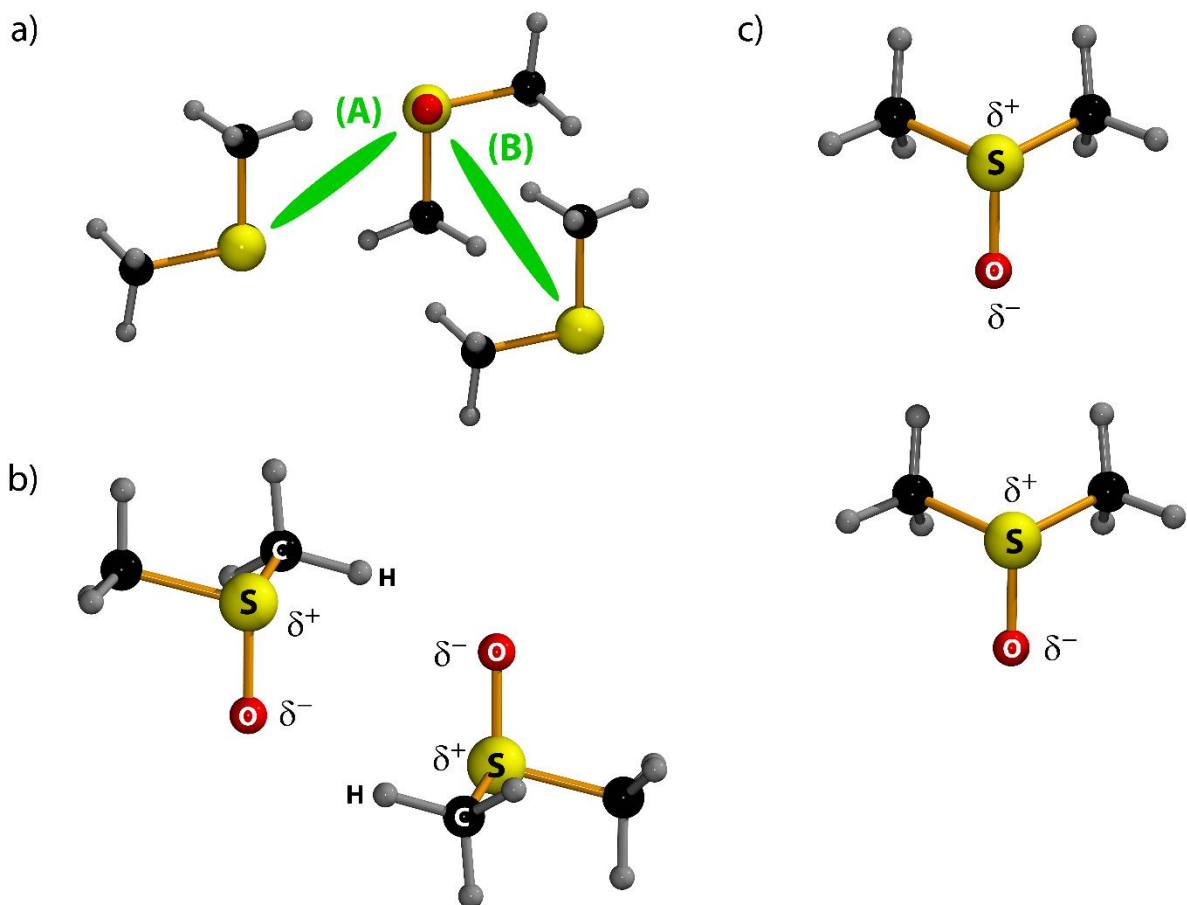
869

870

871 **Figure 13**

872 Illustration of the DMSO–water chain in DMSO trihydrate, viewed approximately  
 873 perpendicular to the  $(\bar{1}01)$  plane, showing the crankshaft-like arrangement of  $\text{O}-\text{H}\cdots\text{O}$   
 874 hydrogen bonds (red dashed rods) and the supporting  $\text{C}-\text{H}\cdots\text{O}$  hydrogen bond (green dashed  
 875 rods), forming a polygonal tape along  $b$ . Symmetry codes: (i)  $-x, \frac{1}{2}+y, \frac{1}{2}-z$ ; (ii)  $x, 1+y, z$ ; (iii)  
 876  $-x, -\frac{1}{2}+y, \frac{1}{2}-z$ .

877



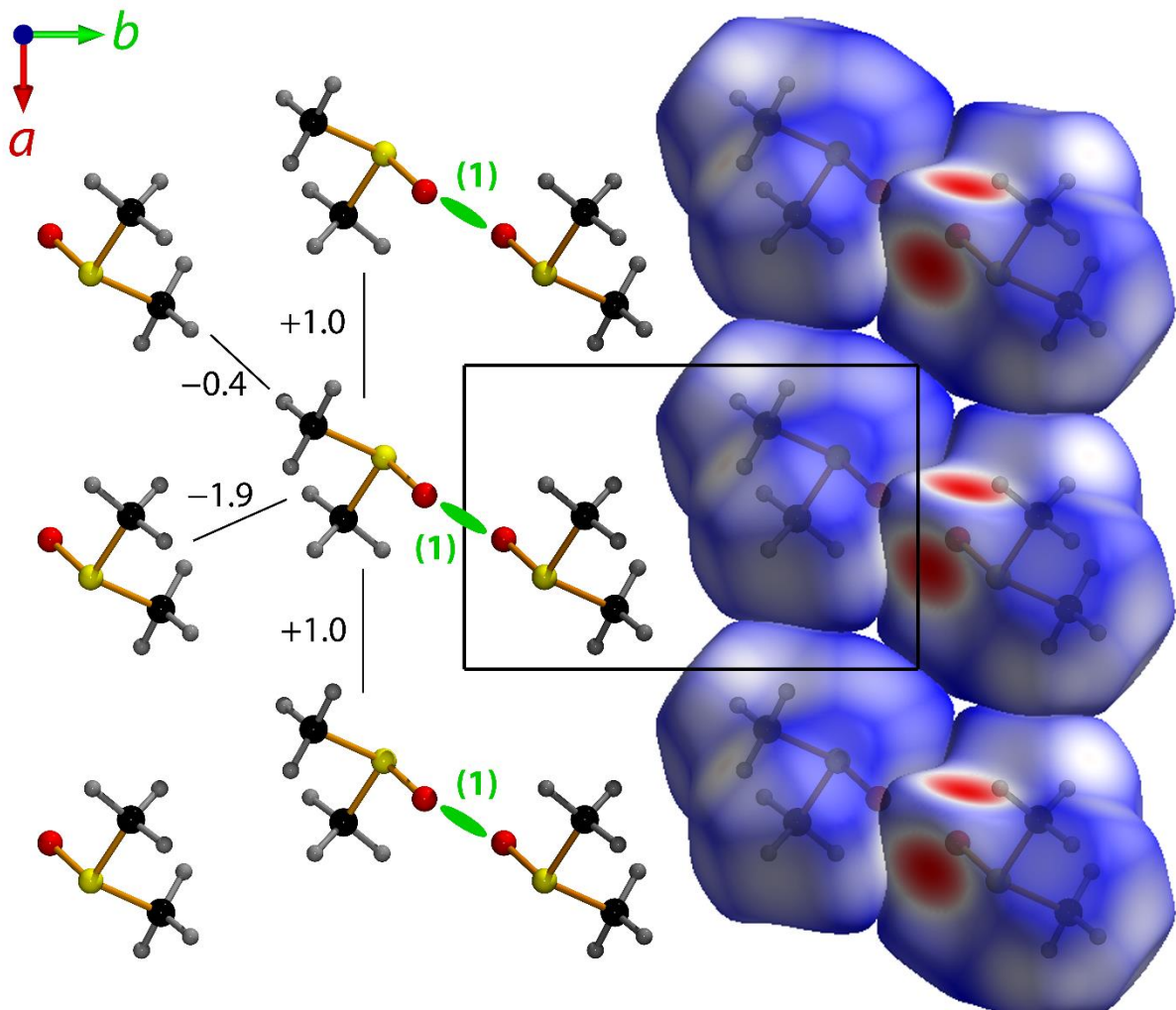
878

879

880 **Figure 14**

881 Possible arrangements of O–S dipoles between pairs of DMSO molecules. (a) Two types of  
 882 antiparallel ordering of the dipoles occurs in solid DMSO; the first, marked A, is found where  
 883 the pyramidal edges of the O–S–C molecule are aligned; the second, marked B, occurs where  
 884 the pyramidal bases face one another. The type-A antiparallel interaction is illustrated in (b) to  
 885 highlight the possible C–H···O hydrogen bonding. (c) Parallel arrangements of the dipoles  
 886 allow only the electrostatic interaction with no hydrogen bonding being possible.

887



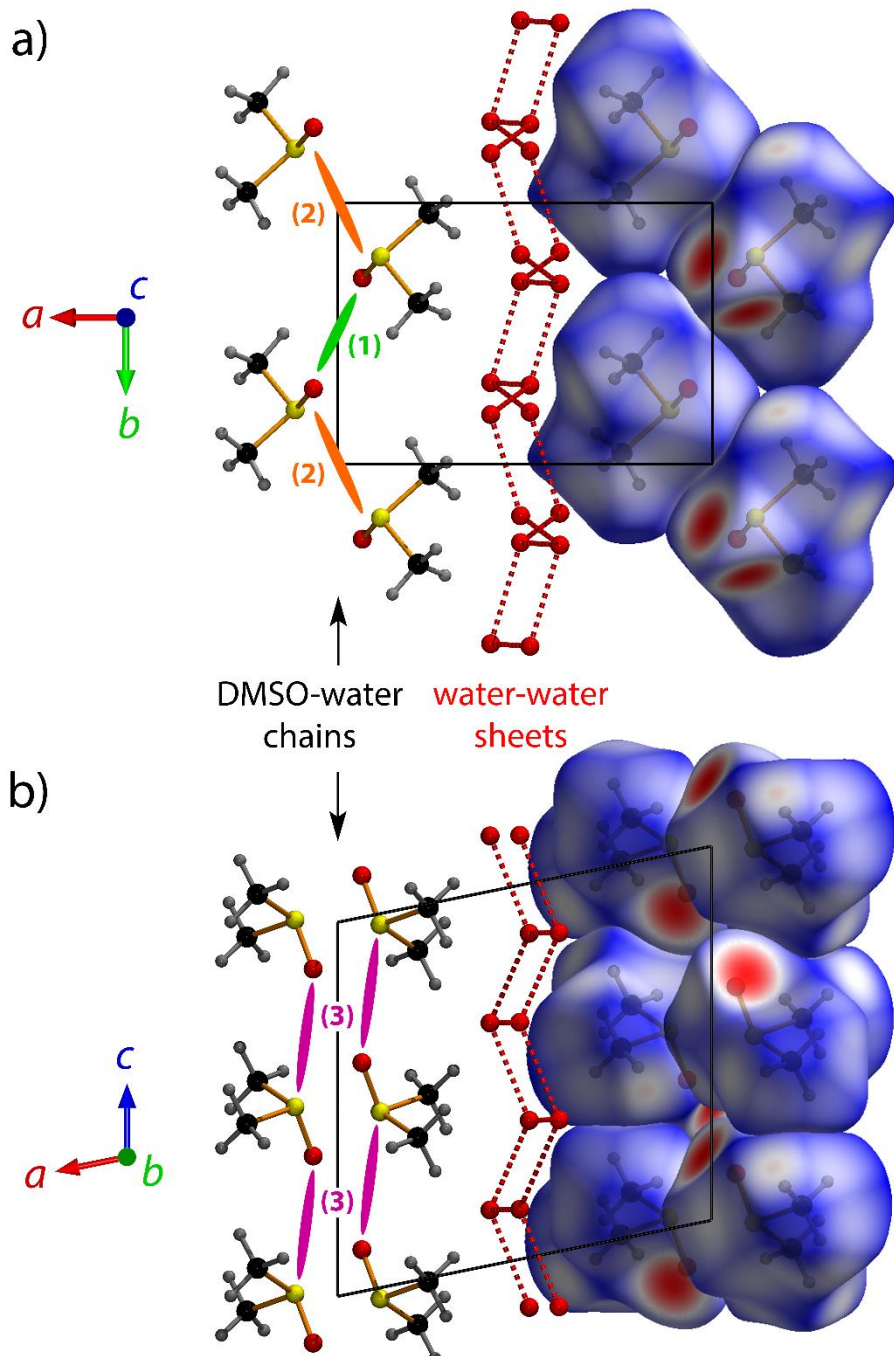
888

889

890 **Figure 15**

891 DMSO molecules in the interlocking sheet at  $z = \frac{1}{2}$ , viewed along the *c*-axis. The packing of  
 892 the Hirschfeld surfaces is shown on the right, and the electrostatic interactions on the left. The  
 893 green lozenge indicates the strong interaction between antiparallel dipoles (see Table 4); the  
 894 remaining very weak interactions are marked with solid black lines annotated with the total  
 895 energy of the interaction determined by CrystalExplorer (see main text).

896



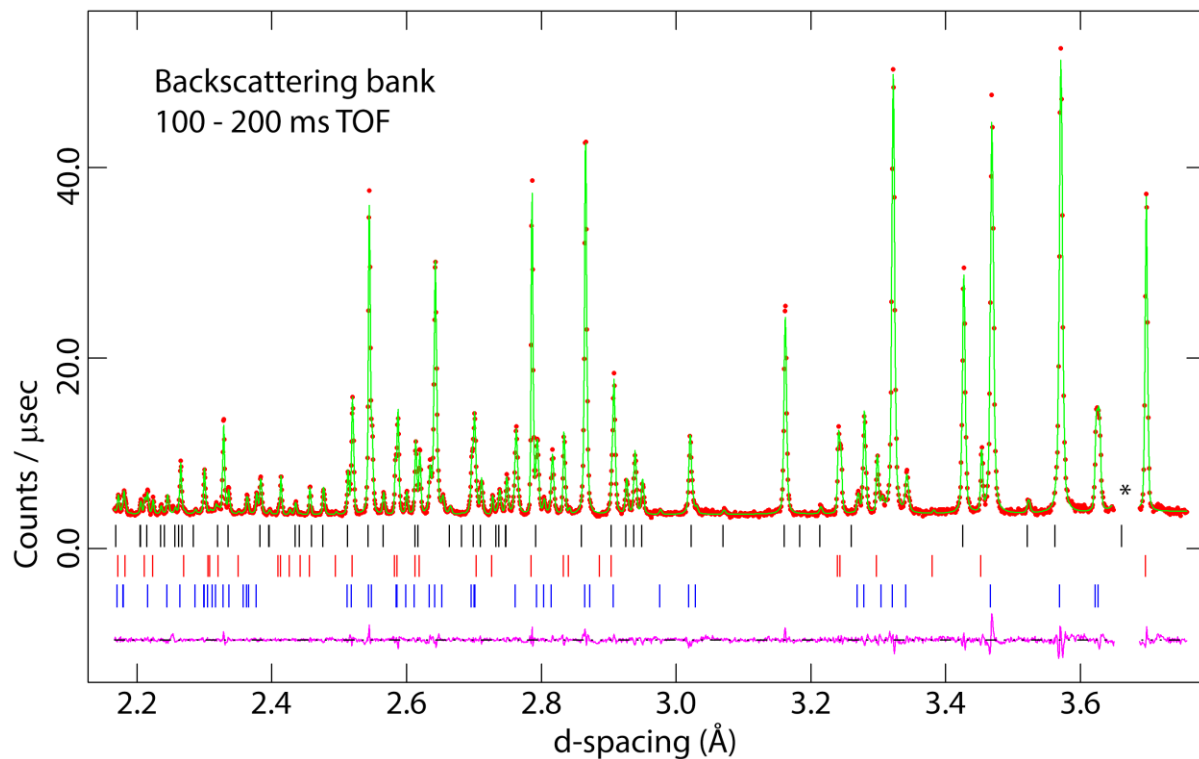
897

898

899 **Figure 16**

900 DMSO molecules in the interlocking chains at  $x = 0$ , viewed along the  $c$ -axis (top) and the  $b$ -  
 901 axis (bottom). The packing of the Hirschfeld surfaces is shown on the right, and the electrostatic  
 902 interactions on the left. The green and orange lozenges, numbered (1) and (2) respectively,  
 903 indicate the zig-zag chain of interactions between antiparallel dipoles. The purple lozenges,  
 904 numbered (3), indicate the parallel dipole interactions. The geometries and estimated energies  
 905 of these interactions are given in Table 4. Note that the water molecules in the chains have been  
 906 omitted for clarity and the hydrogen atoms of the water-water sheet (red spheres and dashed  
 907 rods) at  $x = \frac{1}{2}$  are also omitted.

908



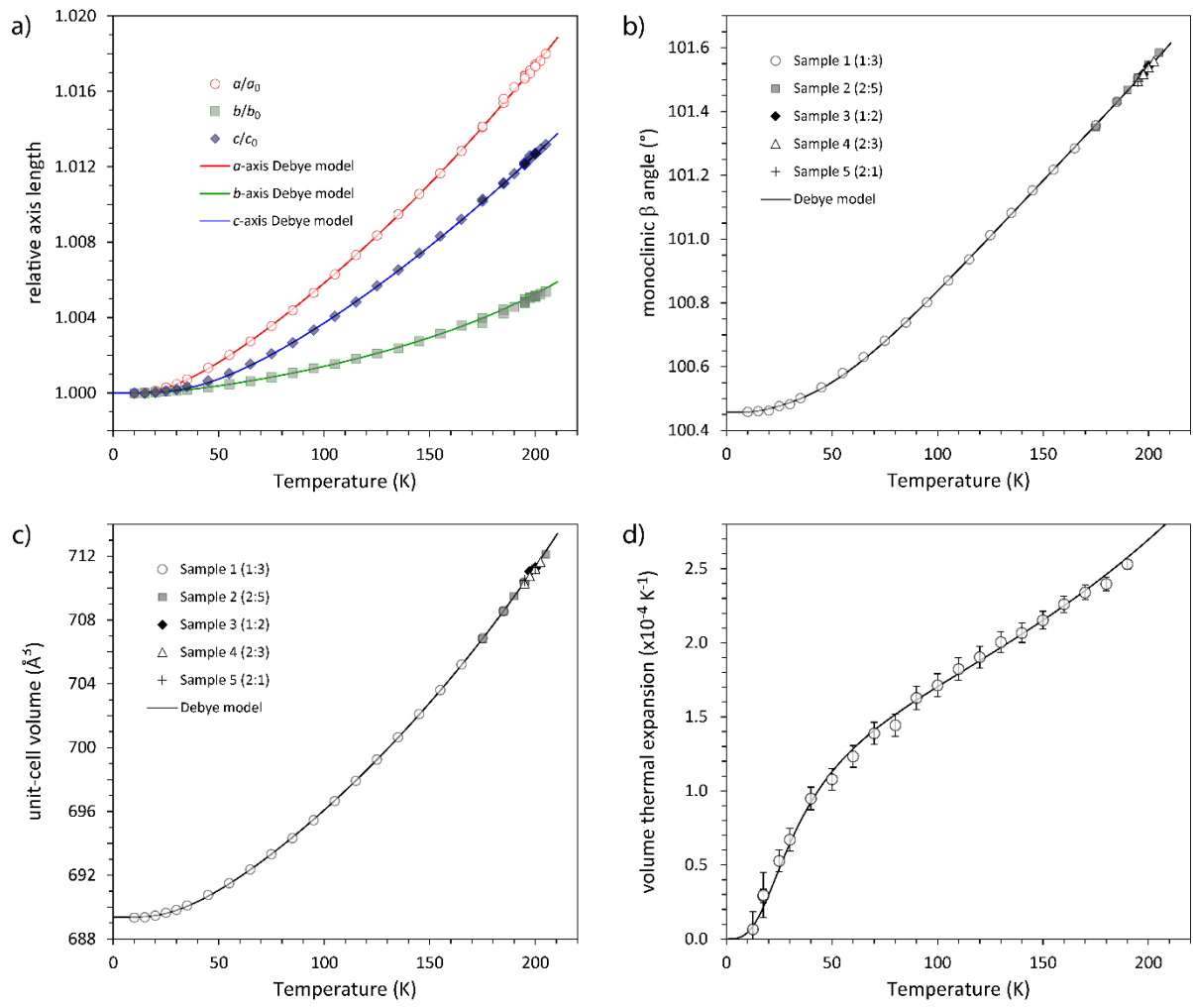
909

910

911 **Figure 17**

912 Neutron powder diffraction pattern of Sample-4 at 175 K on its second thermal cycle. Red  
 913 circles mark the observations, the green line is a LeBail-calculated best fit and the purple line  
 914 underneath is the difference between the observations and the fit. The data contains  
 915 contributions from three crystalline phases whose peak positions are indicated by the vertical  
 916 tick marks underneath the diffraction pattern: the upper black tick marks represent  $\beta$ -DMSO  
 917 dihydrate, the middle red tick marks indicate anhydrous DMSO; the lower blue tick marks  
 918 represent  $\alpha$ -DMSO dihydrate. An asterisk marks one small excluded regions where a weak,  
 919 broad peak of unknown origin as present.

920



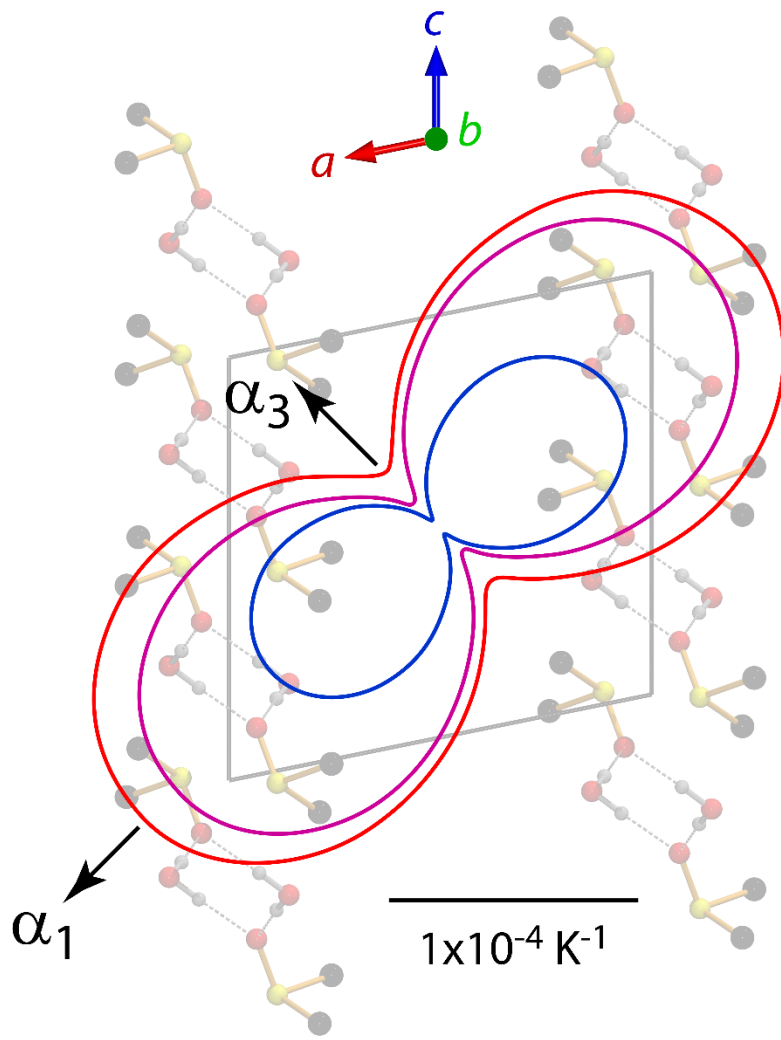
921

922

### 923 **Figure 18**

924 (a) Relative lengths of the unit-cell edges in DMSO-*d*<sub>6</sub>·3D<sub>2</sub>O, referenced to the measurement  
 925 at 10 K. Symbols report values given in Suppl. Table S2 and the solid lines represent the 2<sup>nd</sup>-  
 926 order Debye model fit (Suppl. Table S3). Absolute values of (b) the monoclinic angle  $\beta$  and  
 927 (c) the unit-cell volume of DMSO-*d*<sub>6</sub>·3D<sub>2</sub>O as a function of temperature. (d) The coefficient of  
 928 volume thermal expansion derived from the observed lattice parameters (symbols) and from  
 929 the Debye model (solid line).

930



931

932

933 **Figure 19**

934 Sections in the  $a$ - $c$  plane of the thermal expansion tensor of DMSO- $d_6 \cdot 3D_2O$  at three different  
 935 temperatures: 50 K (blue); 120 K (purple); 190 K (red). The orientations of the principal  
 936 direction that are not constrained by symmetry,  $\alpha_1$  and  $\alpha_3$  are marked, and the diagram is laid  
 937 over the structure of DMSO trihydrate projected along the  $b$ -axis, showing only the DMSO-  
 938 water chains.

939

940

941 **TABLES**

942

943 **Table 1**

944

945 Internal geometry of the DMSO-*d*<sub>6</sub> molecule in the anhydrous solid (Ibberson, 2005) and in  
946 the two hydrates reported here. Note that Ibberson used a slightly different labelling scheme  
947 from the one we have employed for the methyl deuterons.

948

	DMSO- <i>d</i> <sub>6</sub> 100 K		DMSO- <i>d</i> <sub>6</sub> ·2D <sub>2</sub> O 175 K	DMSO- <i>d</i> <sub>6</sub> ·3D <sub>2</sub> O 195 K
O–S	1.496(2)	O–S	1.501(8)	1.516(5)
S–C1	1.838(3)	S–C1	1.787(8)	1.765(6)
S–C2	1.788(3)	S–C2	1.788(9)	1.794(6)
C1–D11	1.080(2)	C1–D1	1.107(6)	1.074(4)
C1–D21	1.076(2)	C1–D2	1.070(7)	1.089(4)
C1–D31	1.076(2)	C1–D3	1.082(6)	1.085(4)
C2–D12	1.088(2)	C2–D4	1.092(5)	1.073(4)
C2–D22	1.095(2)	C2–D5	1.079(5)	1.081(4)
C2–D32	1.073(2)	C2–D6	1.102(5)	1.084(4)
O–S–C1	105.2(1)	O–S–C1	106.0(5)	105.6(3)
O–S–C2	108.3(1)	O–S–C2	105.5(5)	104.9(3)
C1–S–C2	96.4(1)	C1–S–C2	97.9(4)	97.9(3)
D11–C1–D21	111.4(1)	D1–C1–D2	108.6(7)	110.2(4)
D11–C1–D31	113.7(2)	D1–C1–D3	115.0(8)	109.1(4)
D21–C1–D31	112.6(2)	D2–C1–D3	115.5(9)	111.5(5)
D12–C2–D22	111.0(1)	D4–C2–D5	109.5(6)	110.8(5)
D12–C2–D32	112.5(1)	D4–C2–D6	112.6(5)	110.6(4)
D22–C2–D32	112.4(1)	D5–C2–D6	109.7(6)	111.3(5)

949

950

951

952

953 **Table 2**

954

955 Geometry of the hydrogen bonds in  $\alpha$ -DMSO dihydrate. The C–H $\cdots$ O contacts are assigned  
956 tentatively on the basis of distances and particularly the linearity.

957

	D–H ( $\text{\AA}$ )	H $\cdots$ A ( $\text{\AA}$ )	D $\cdots$ A ( $\text{\AA}$ )	D–H $\cdots$ A ( $^\circ$ )
Ow1–Dw1a $\cdots$ O1	0.970(7)	1.829(5)	2.798(6)	176.6(6)
Ow1–Dw1b $\cdots$ Ow2 <sup>(i)</sup>	0.933(7)	1.806(7)	2.731(8)	171.5(5)
Ow2–Dw2a $\cdots$ O1	0.970(7)	1.787(6)	2.751(7)	172.5(5)
Ow2–Dw2b $\cdots$ Ow1 <sup>(ii)</sup>	0.962(7)	1.823(6)	2.780(8)	172.5(5)
C2–D4 $\cdots$ Ow2 <sup>(iii)</sup>	1.092(7)	2.527(7)	3.567(7)	159.0(5)
C2–D6 $\cdots$ Ow2 <sup>(iv)</sup>	1.103(7)	2.544(8)	3.638(7)	171.5(5)

958

959 Symmetry codes

960 (i)  $1+x, y, z$ ; (ii)  $1-x, -\frac{1}{2}+y, \frac{1}{2}-z$ ; (iii)  $x, 1\frac{1}{2}-y, -\frac{1}{2}+z$ ; (iv)  $1-x, \frac{1}{2}+y, \frac{1}{2}-z$ .

961

962 **Table 3**

963

964 Geometry of the hydrogen bonds in DMSO trihydrate. The C–H $\cdots$ O contacts are assigned  
965 tentatively on the basis of distances and particularly the linearity.

966

	D–H ( $\text{\AA}$ )	H $\cdots$ A ( $\text{\AA}$ )	D $\cdots$ A ( $\text{\AA}$ )	D–H $\cdots$ A ( $^\circ$ )
Ow1–Dw1a $\cdots$ Ow2 <sup>(i)</sup>	0.976(5)	1.876(5)	2.834(5)	166.6(4)
Ow1–Dw1b $\cdots$ Ow2	0.986(7)	1.796(7)	2.781(7)	179.2(5)
Ow2–Dw2a $\cdots$ Ow3	0.972(6)	1.741(6)	2.701(7)	168.6(5)
Ow2–Dw2b $\cdots$ Ow1 <sup>(ii)</sup>	0.989(6)	1.788(6)	2.772(7)	172.6(5)
Ow3–Dw3a $\cdots$ O1	0.979(6)	1.805(5)	2.784(6)	179.5(4)
Ow3–Dw3b $\cdots$ O1 <sup>(iii)</sup>	0.945(5)	1.786(5)	2.730(5)	176.5(4)
C1–D1 $\cdots$ Ow3 <sup>(iv)</sup>	1.074(5)	2.529(6)	3.585(6)	167.5(4)
C1–D2 $\cdots$ Ow1	1.089(6)	2.561(7)	3.645(6)	173.0(4)
C2–D4 $\cdots$ O1 <sup>(v)</sup>	1.073(6)	2.622(6)	3.661(5)	162.9(4)

967

968 Symmetry codes

969 (i)  $1-x, 1-y, 1-z$ ; (ii)  $1-x, -\frac{1}{2}+y, \frac{1}{2}-z$ ; (iii)  $-x, -\frac{1}{2}+y, \frac{1}{2}-z$ ; (iv)  $x, 1+y, z$ ; (v)  $-x, 1-y, 1-z$

970 **Table 4**

971

972 Geometry of the various dipole-dipole interactions in solid DMSO-*d*<sub>6</sub> (Ibberson, 2005) and the  
 973 two hydrates reported here. AP = antiparallel, where the (A) and (B) denote the edge-on and  
 974 face-on interactions shown in Figure 14a; P = parallel. The total interaction energies, *E*<sub>TOT</sub>,  
 975 from Crystal Explorer are decomposed into electrostatic (*E*<sub>ele</sub>), polarisation (*E*<sub>pol</sub>), dispersion  
 976 (*E*<sub>disp</sub>) and exchange-repulsion (*E*<sub>rep</sub>) terms.

977

	DMSO- <i>d</i> <sub>6</sub>			DMSO- <i>d</i> <sub>6</sub> ·3D <sub>2</sub> O			α-DMSO- <i>d</i> <sub>6</sub> ·2D <sub>2</sub> O
	100 K			195 K			175 K
Type	AP (A)	AP (B)	P	AP (A)	AP (A)	P	AP (A)
O···O (Å)	3.964(2)	4.401(2)	5.239(2)	4.159(5)	4.911(4)	5.058(4)	3.473(6)
S···S (Å)	4.122(4)	5.051(3)	5.239(3)	4.754(8)	3.634(9)	5.079(7)	4.051(10)
O···S (Å)	3.636(3)	4.495(3)	3.792(2)	4.201(7)	4.045(7)	3.752(6)	3.461(9)
S–O···S (°)	98.1(1)	103.2(1)	162.6(1)	102.0(3)	63.6(2)	145.9(3)	102.1(3)
S–O···S–O (°)	−4.8(2)	0.0(1)	180.0(5)	0.0(4)	0.0(4)	−96.8(8)	0.0(4)
<i>E</i> <sub>ele</sub> (kJ mol <sup>−1</sup> )	−22.6	−24.8	−19.4	−19.3	−10.7	−1.4	−25.7
<i>E</i> <sub>pol</sub> (kJ mol <sup>−1</sup> )	−5.5	−6.9	−5.9	−4.4	−1.3	−2.7	−7.4
<i>E</i> <sub>disp</sub> (kJ mol <sup>−1</sup> )	−10.7	−13.9	−7.2	−7.3	−8.3	−7.5	−11.6
<i>E</i> <sub>rep</sub> (kJ mol <sup>−1</sup> )	+17.8	+22.1	+14.6	+7.4	+8.7	+5.2	+17.5
<i>E</i> <sub>TOT</sub> (kJ mol <sup>−1</sup> )	−26.2	−29.6	−22.1	−25.4	−14.1	−6.8	−31.9

978

On the crystal structures and phase transitions of hydrates in the  
binary system, dimethyl sulfoxide (DMSO) – water.

Supplementary Figures and Tables

A. D. Fortes,<sup>1</sup> J. Ponsonby,<sup>1,2</sup> O. Kirichek,<sup>1</sup> V. García-Sakai<sup>1</sup>

<sup>1</sup>ISIS Pulsed Neutron and Muon Source, Rutherford Appleton Laboratory, Harwell Science and Innovation Campus, Chilton, Oxfordshire OX11 0QX

<sup>2</sup>Faculty of Science, University of Bath, Claverton Down, Bath, Somerset BA2 7AY, United Kingdom.

Corresponding author email: [dominic.fortes@stfc.ac.uk](mailto:dominic.fortes@stfc.ac.uk)

## Supplementary Figures

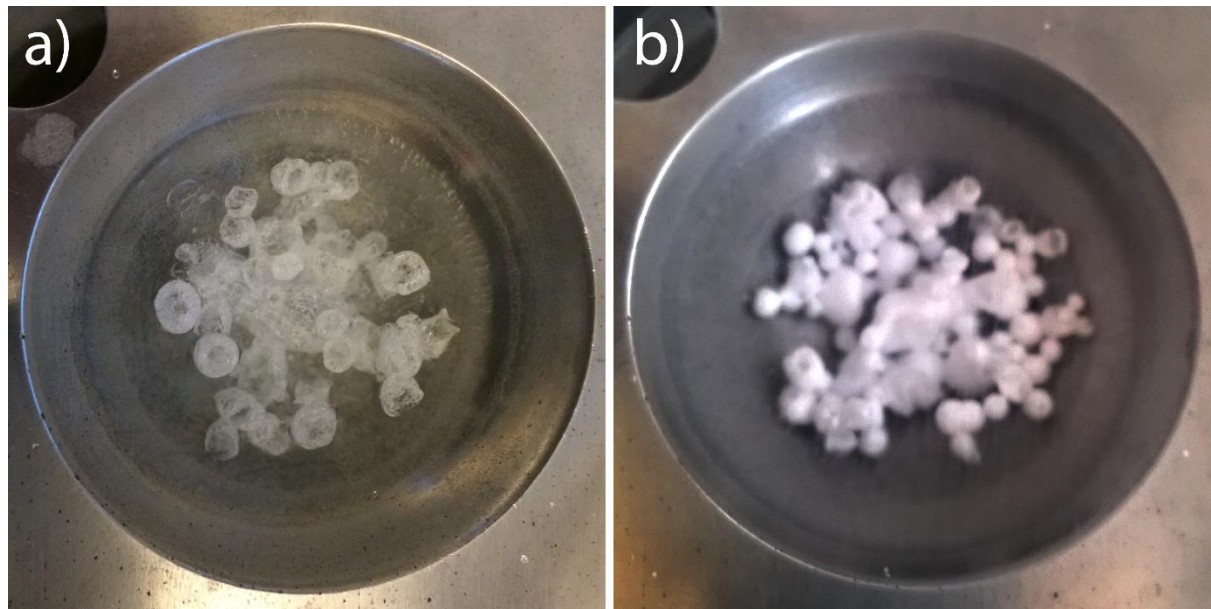


**Figure S1**

Photographs of sample-1 (left) and sample-5 (right) immediately after freezing of the aqueous solution droplets in liquid nitrogen. Notice that the spherules in sample-1 are transparent and slightly larger (3.5 – 5.5 mm) than the opaque sample-5 spherules (2.0 – 5.0 mm). The steel cryomortar holding the samples has a bowl diameter of 65.5 mm, a depth of 21 mm, and volume of 40.2 cm<sup>3</sup>.

Sample 1 (DMSO-d<sub>6</sub> : D<sub>2</sub>O = 1 : 3), cooling

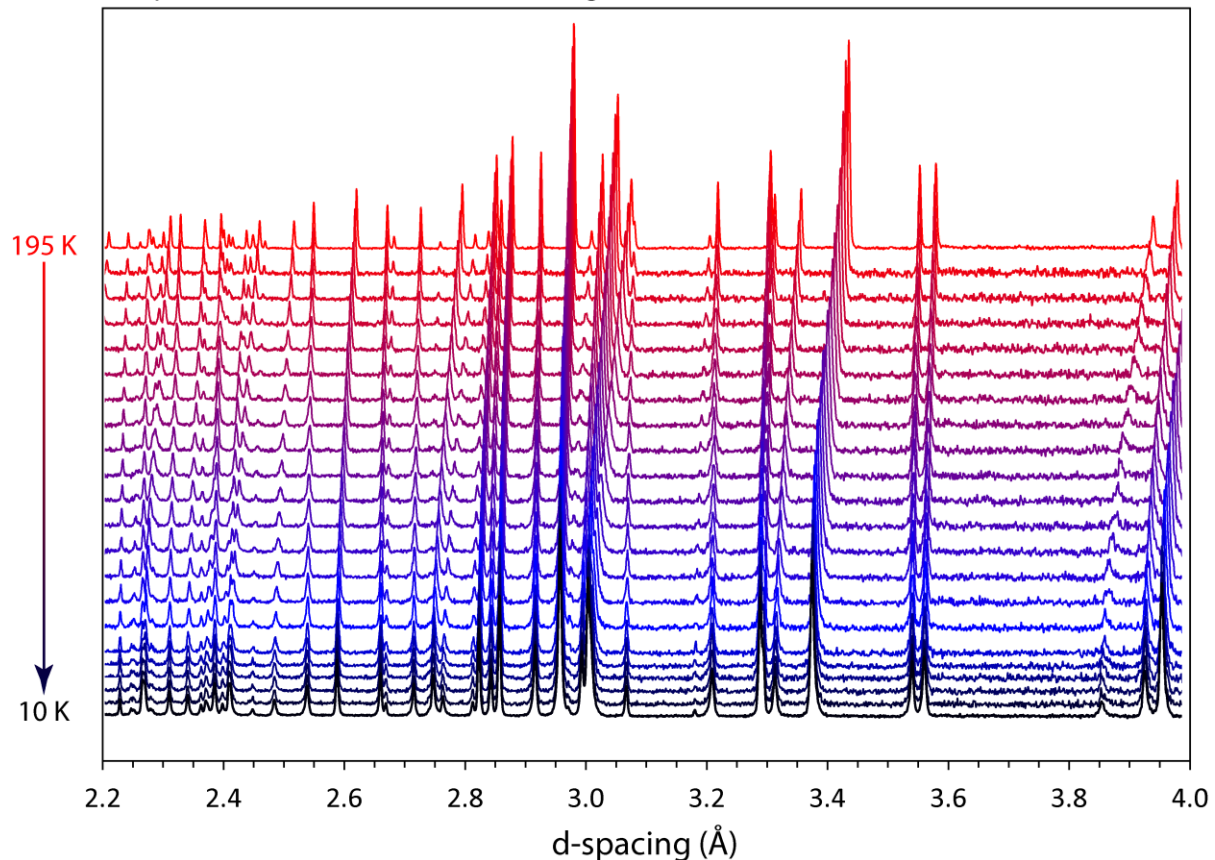


**Figure S2a**

Stackplot of neutron powder diffraction data collected from sample-1 (phase pure DMSO trihydrate) on cooling from 195 K (top) to 10 K (bottom). As expected, peaks shift to shorter d-spacings due to contraction of the unit cell on cooling, but the shifts are not uniform by virtue of the crystal's anisotropy.

Sample 1 (DMSO-d<sub>6</sub> : D<sub>2</sub>O = 1 : 3), cooling

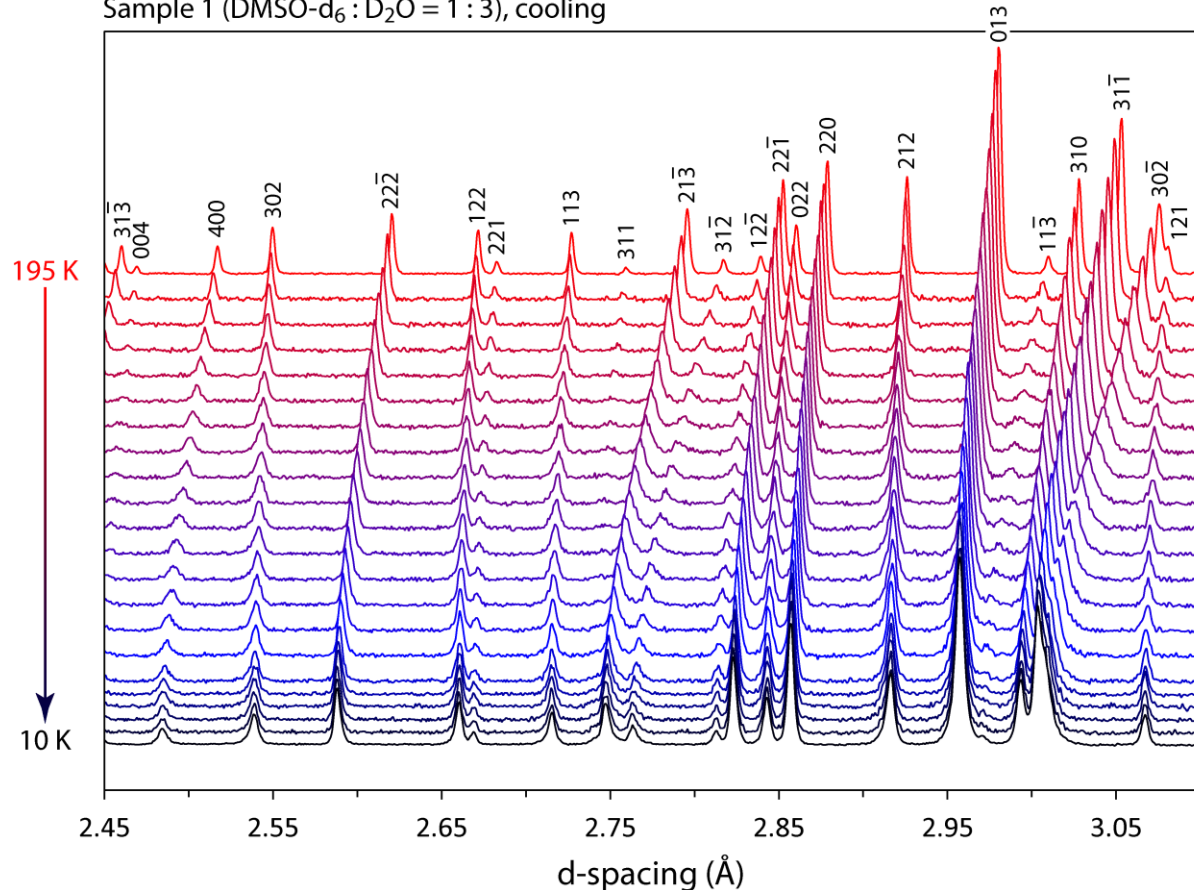


**Figure S2b**

An expanded view of Figure S2a with the diffraction indices of each Bragg peak marked. This gives a clearer illustration of the peak broadening that occurs on cooling.

Sample 2 (DMSO-d<sub>6</sub> : D<sub>2</sub>O = 2 : 5), heating and cooling

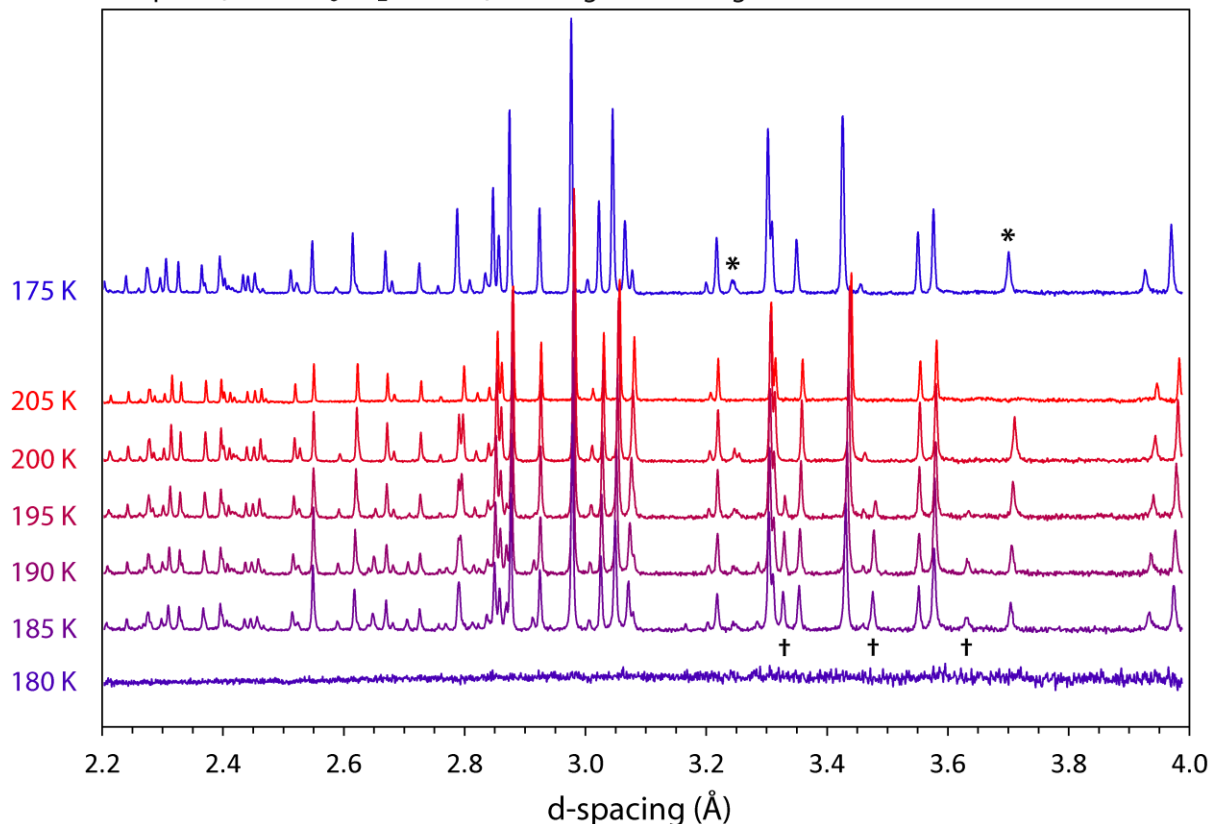


**Figure S3**

Stackplot of neutron powder diffraction data collected from sample-2, starting from the amorphous phase (exhibiting no Bragg peaks) at 180 K, followed by crystallisation and a series of phase transitions on warming to 205 K. The uppermost diffraction pattern was acquired after cooling back to 175 K. Asterisks mark the strongest peaks from anhydrous DMSO, which disappear at 205 K due to partial melting, and reappear at 175 K by freezing of the partial melt. The dagger symbols mark the strongest Bragg peaks from α-DMSO dihydrate.

Sample 3 (DMSO-d<sub>6</sub> : D<sub>2</sub>O = 1 : 2), heating

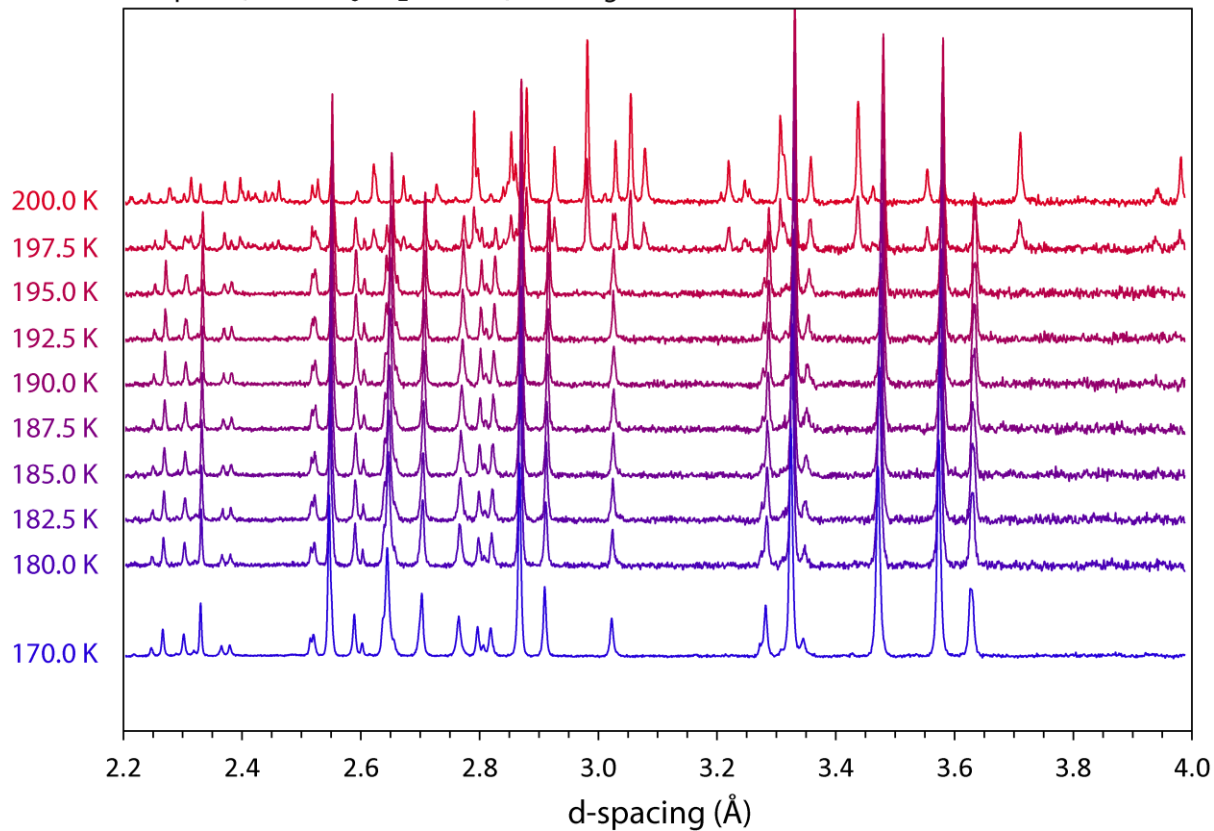


**Figure S4**

Stackplot of neutron powder diffraction data collected from sample-3, which – after crystallisation – consists of phase-pure  $\alpha$ -DMSO dihydrate. An abrupt phase transition to a mixture of DMSO and DMSO trihydrate is evident from the change in the diffraction pattern at 197.5 and 200 K.

Sample 4 (DMSO-d<sub>6</sub> : D<sub>2</sub>O = 2 : 3), Initial heating

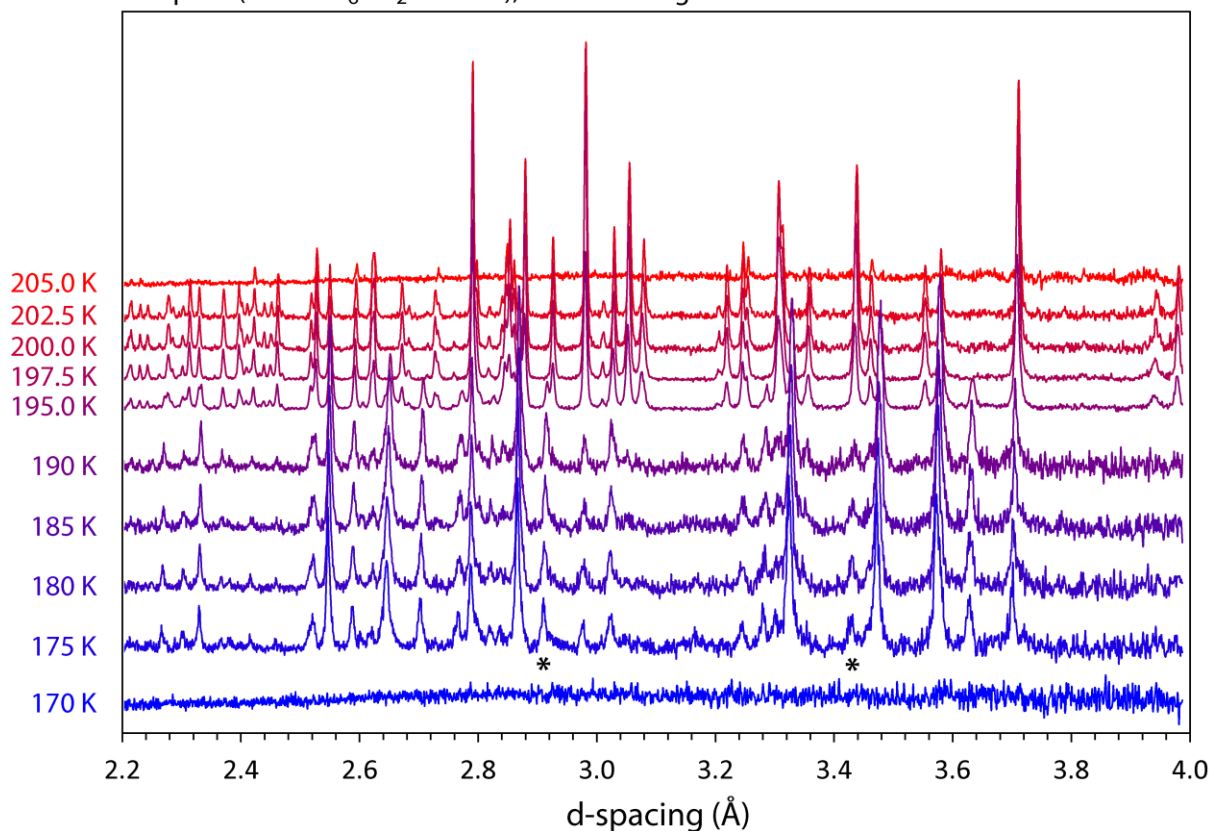


**Figure S5**

Stackplot of neutron powder diffraction data collected from sample-4 during its first heating cycle. The initially amorphous phase at 170 K transforms on heating to a mixture of crystalline DMSO,  $\alpha$ -DMSO dihydrate and some DMSO trihydrate (peaks marked with asterisks). Between 190 and 195 K, the dihydrate phase transforms completely to trihydrate + DMSO, and then undergoes partial melting to DMSO + liquid between 202.5 and 205 K.

Sample 4 (DMSO-d<sub>6</sub> : D<sub>2</sub>O = 2 : 3), Second heating

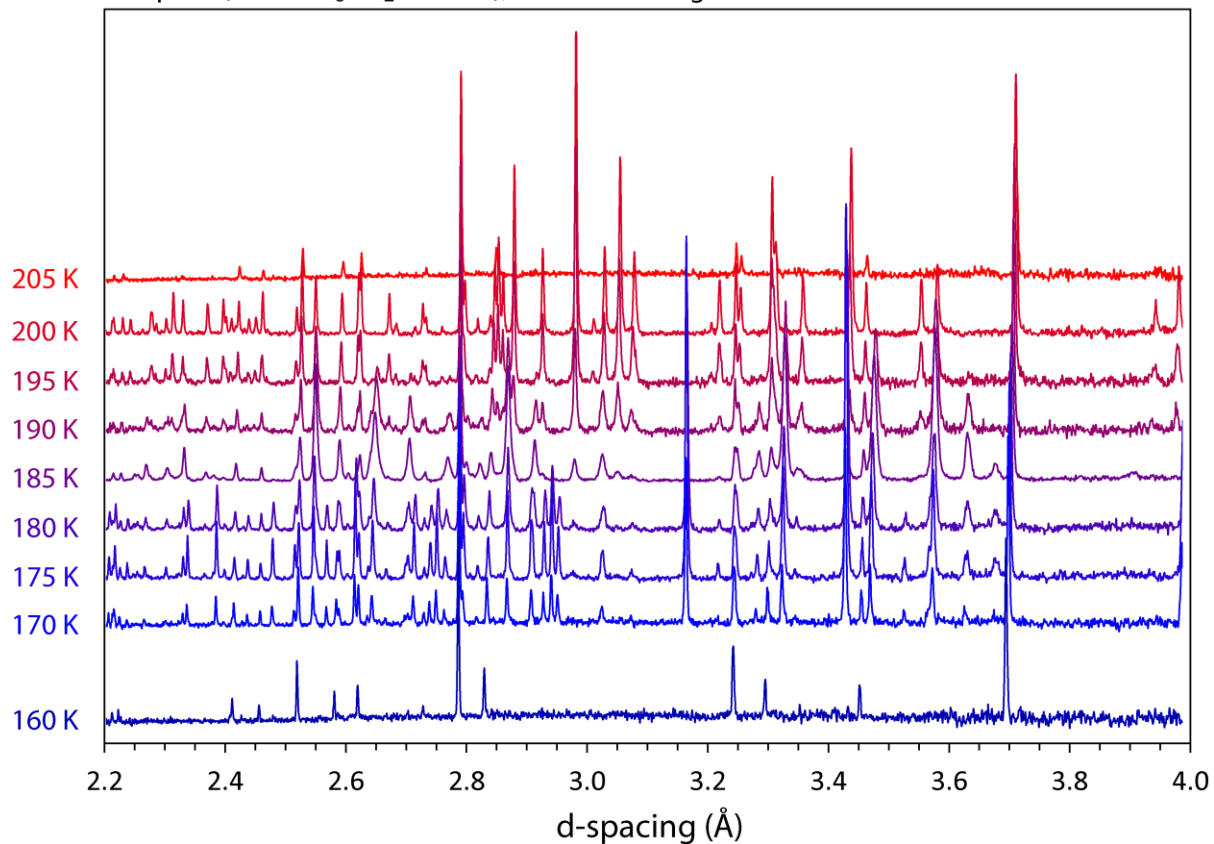


**Figure S6**

Stackplot of neutron powder diffraction data collected from sample-4 during its second heating cycle. The sample shown at 205 K in Figure S5 was rapidly cooled to 100 K; subsequent warming to 160 K (bottom trace here) shows it to contain only crystalline DMSO as well as an amorphous residue. At 170 K, the amorphous residue crystallises into  $\beta$ -DMSO dihydrate with some  $\alpha$ -dihydrate. The beta phase persists up to 180 K; the remaining  $\alpha$ -dihydrate once again breaks down to DMSO + DMSO trihydrate between 190 and 195 K.

Sample 5 (DMSO-d<sub>6</sub> : D<sub>2</sub>O = 2 : 1), heating

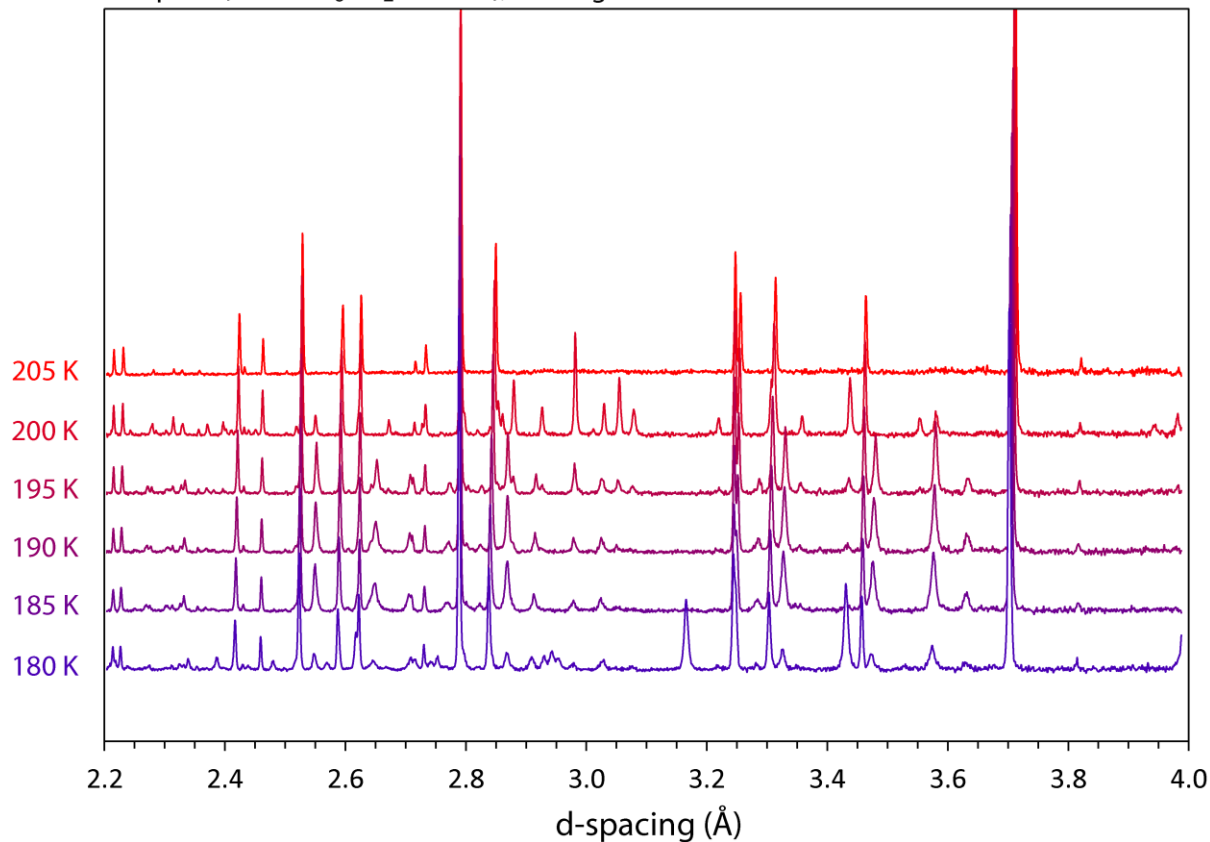


**Figure S7**

Stackplot of neutron powder diffraction data collected from sample-5. This specimen was already partially crystalline at 100 K, containing DMSO + glass. Warming to 180 K resulted in the amorphous component crystallising into a mixture of  $\alpha$ - and  $\beta$ -DMSO dihydrate. The  $\beta$ -dihydrate was absent on warming to 185 K, and the remaining  $\alpha$ -dihydrate underwent a reaction to DMSO + DMSO trihydrate during further warming, which was complete by 200 K. At 205 K, we observed a partially molten mixture of DMSO + liquid.

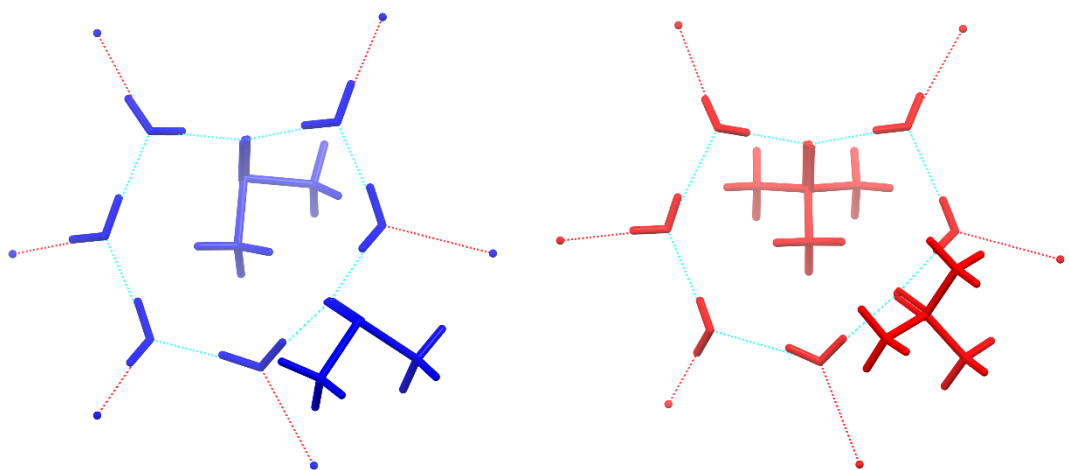


**Figure S8**

Schematic illustration of the  $R_8^6(16)$  rings in  $\alpha$ -DMSO dihydrate (left, in blue) and in trimethylamine N-oxide (TMAO) dihydrate (right, in red). Molecules are drawn as solid rods; dashed turquoise lines depict the hydrogen bonds in the ring, and red dashed lines show the H-bonds forming partial adjacent rings. The DMSO and TMAO molecules are shown in the 12 o'clock position (pointed inwards and below the ring plane) and the 4 o'clock position (projected outwards and above the ring plane). The scale of both illustrations is identical.

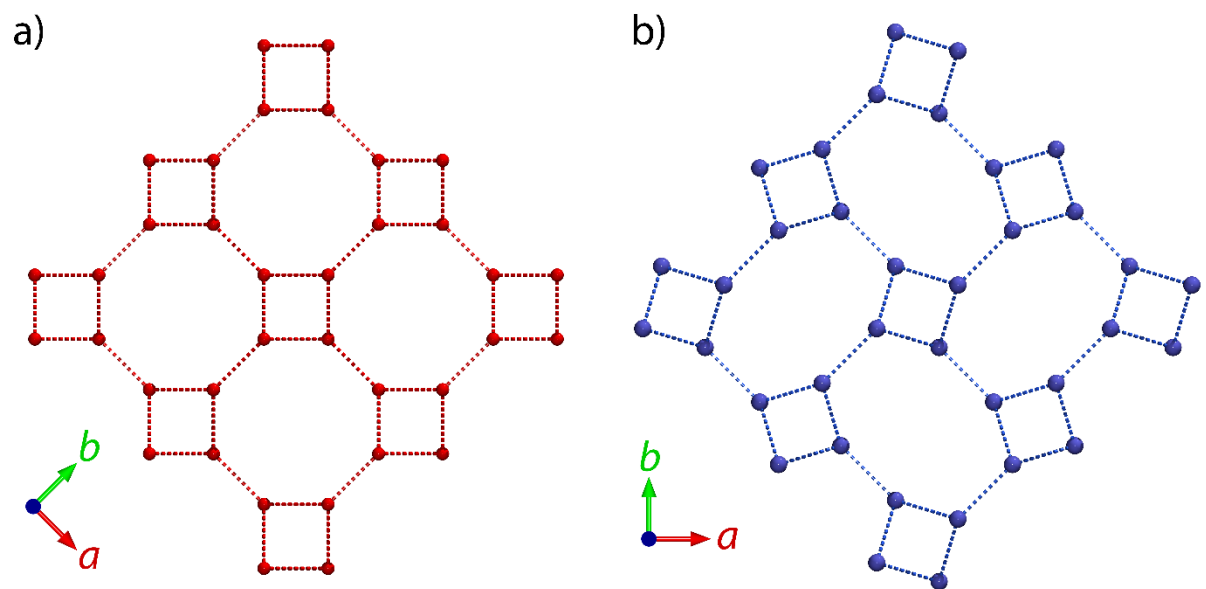


**Figure S9**

Nodal connectivity of the sheets from one of the two interpenetrating frameworks in ice VI (left) and the framework of edingtonite (right), showing a similar geometric arrangement of 4-sided and 8-sided rings to that found in the water–water sheets of DMSO trihydrate.

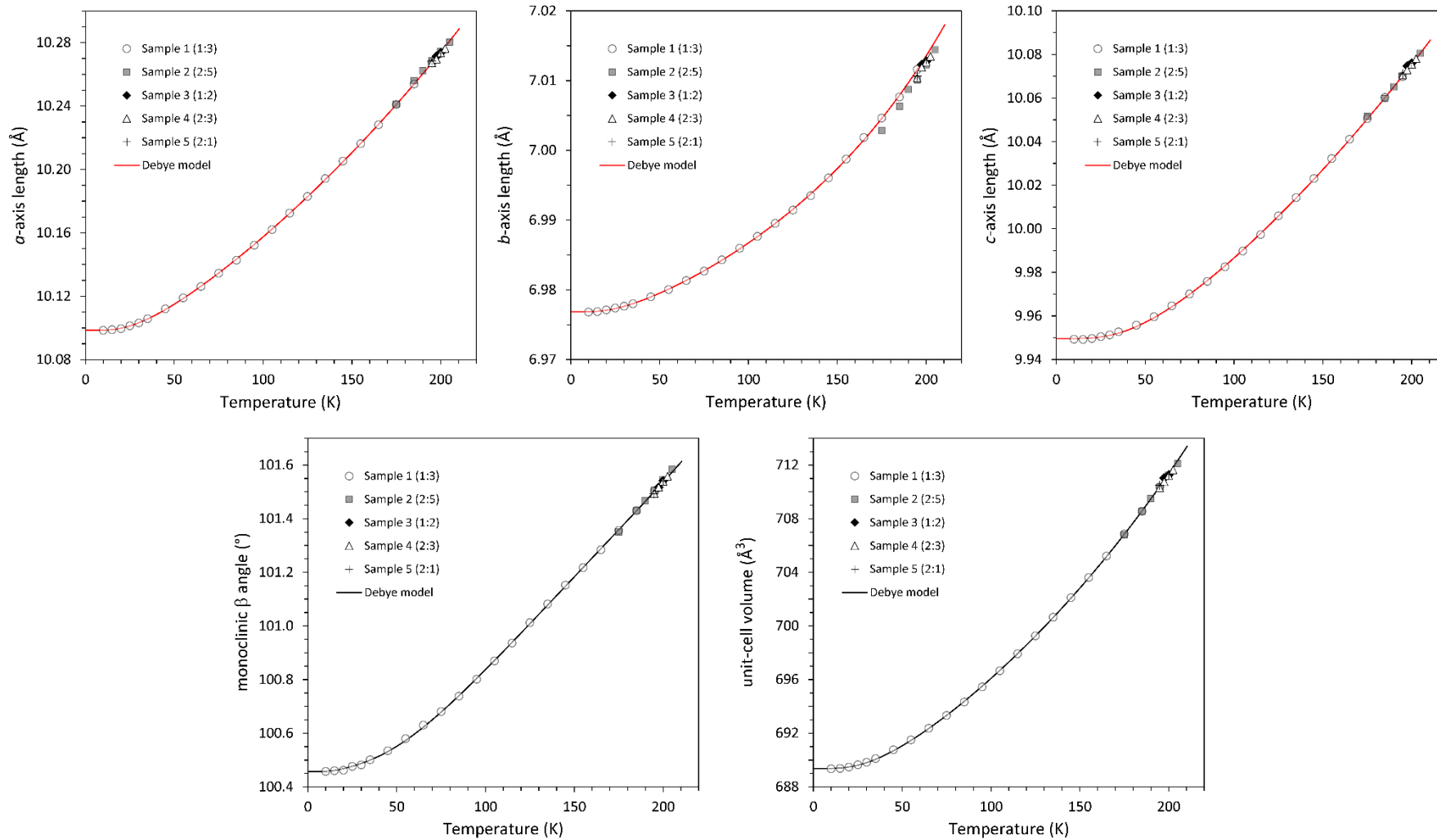


**Figure S10**

Plots of the unit-cell parameters of DMSO- $d_6$ ·3D<sub>2</sub>O using the data reported in Table S2 below. Points between 10 and 195 K from Sample-1 were used to fit the solid lines using a 2<sup>nd</sup>-order Debye model (*cf.*, Table S3). Error bars are smaller than the symbols.

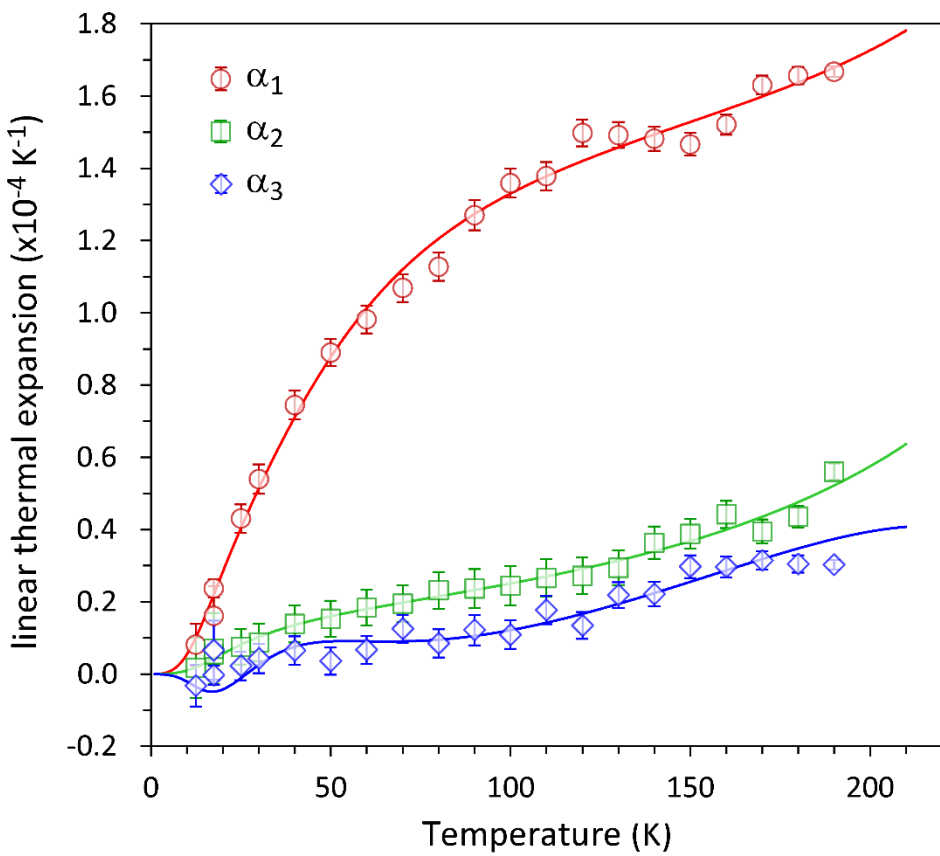


**Figure S11**

Magnitudes of the principal directions of the thermal expansion tensor for DMSO-*d*<sub>6</sub>·3D<sub>2</sub>O as a function of temperature. The direction  $\alpha_2$  is fixed by symmetry along the 2-fold axis of the crystal; the orientation of  $\alpha_1$  and  $\alpha_3$  is shown in the main text, Figure 19. Points are obtained from the refined lattice parameters (Sample-1, 10–195 K) and the solid lines from the fitted 2<sup>nd</sup>-order Debye model.

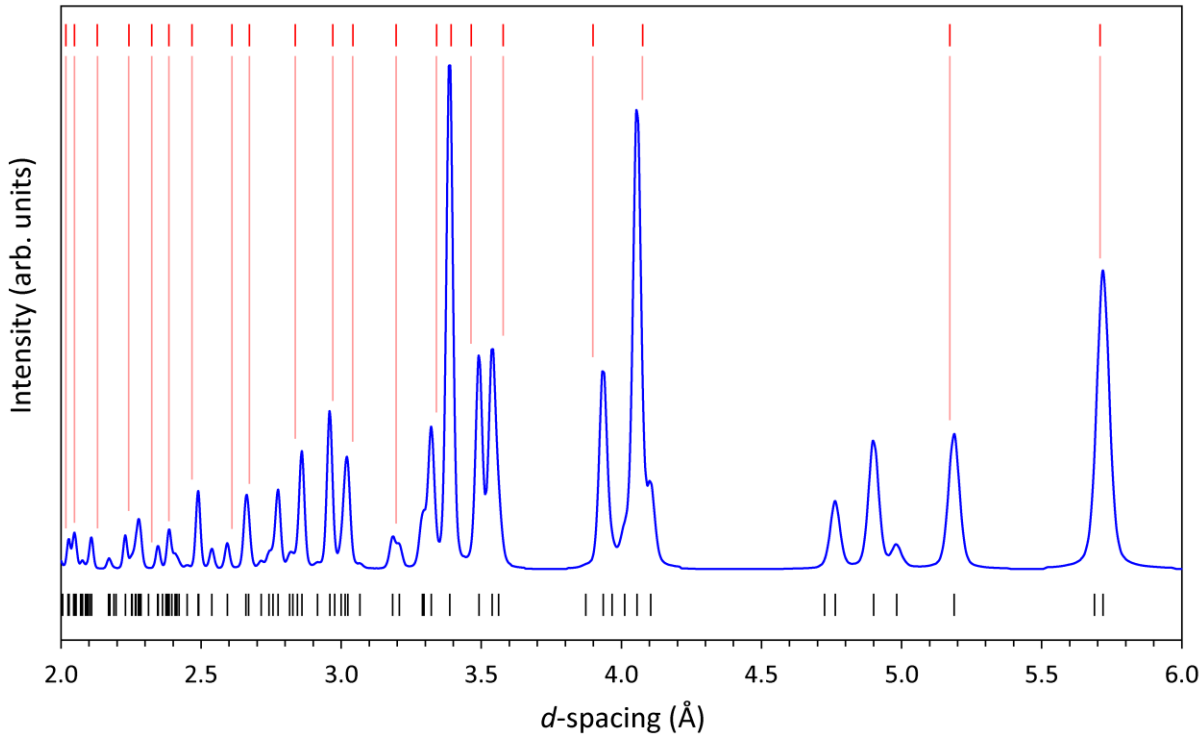


**Figure S12**

Simulated X-ray powder diffraction pattern of DMSO trihydrate (blue line) between 2.0 – 6.0 Å  $d$ -spacing. Reflection positions are marked by the black vertical lines underneath the profile. The red tick marks and pale descending lines above the diffraction pattern show the peak positions tabulated by Boutron & Kaufmann (1978) for their unknown hydrate, observed in flash-frozen 45 wt. % DMSO solution between 77 and 93 K, *after we have subjected the values to a zero shift of  $-0.4^\circ$ .* Note that we have also deliberately broadened the peaks of the simulated pattern to match what we believe the resolution of their system may have been.

There is a reasonably convincing degree of agreement between the simulation and the observed peaks of Boutron & Kaufmann (1978). Some quite strong peaks are ‘missing’, particularly between 4.7 – 5.0 Å and at 10.05 Å (not shown), which are not readily explained. Their experimental setup produced parasitic Bragg peaks from Mylar and beryllium, but these should not mask any intensity from the sample in this region. Equally, the beam-stop evident in Figure 1 of Boutron and Kaufmann’s paper only has an angular radius of  $\sim 5^\circ$ , so cannot account for the missing 10 Å peak.

Nevertheless, we note that the tabulated peaks for ice  $Ih$  in their paper are missing some peaks and are extremely inaccurate, even allowing for a large zero shift, so the degree of agreement we see for the DMSO trihydrate peaks is actually quite good.

## Supplementary Tables

**Table S1**

Refined phase fractions (wt. %) of the phases present in each sample as a function of temperature. Where these could not be determined – because the sample was partially amorphous, or contained a phase with an unknown structure – the table simply notes the presence of phases with a tick.

<b>Sample-1</b>				
T (K)	Amorphous	DMSO·3D <sub>2</sub> O	α-DMSO·2D <sub>2</sub> O	DMSO
195	0	100	0	0
≤ 185	100 (solid)	0	0	0
<b>Sample-2</b>				
T (K)	Amorphous	DMSO·3D <sub>2</sub> O	α-DMSO·2D <sub>2</sub> O	DMSO
205	Liquid	✓	0	0
200	0	90.2	0.0	9.8(2)
195	0	87.2	5.0(1)	7.8(1)
190	0	79.8	13.9(3)	6.3(2)
185	0	79.3	14.6(3)	6.1(2)
≤ 180	100 (solid)	0	0	0
<b>Sample-3</b>				
T (K)	Amorphous	DMSO·3D <sub>2</sub> O	α-DMSO·2D <sub>2</sub> O	DMSO
200.0	0	80.1	0	19.9(3)
197.5	0	35.6	56.0(3)	8.4(2)
175 – 195	0	0	100	0
≤ 170	100 (solid)	0	0	0
<b>Sample-4</b>				
T (K)	Amorphous	DMSO·3D <sub>2</sub> O	α-DMSO·2D <sub>2</sub> O	DMSO
205.0	Liquid	0	0	✓
202.5	0	67.0	0	33.0(3)
200.0	0	69.5	0	30.5(2)
197.5	0	69.4	0	30.6(2)
195	0	44.6	30.9(3)	24.5(2)
190	0	9.7	75(1)	15.3(7)
185	0	9.5	76(1)	14.4(7)
180	0	9.1	77(1)	13.9(7)
175	0	9.0	77(1)	14.0(8)
≤ 170	100 (solid)	0	0	0

**Table S1, continued**

<b>Sample-5</b>				
T (K)	Amorphous	DMSO·3D <sub>2</sub> O	$\alpha$ -DMSO·2D <sub>2</sub> O	DMSO
205	Liquid	0	0	✓
200	0	30.2	0	69.8(3)
195	0	10.4	25.0(3)	64.6(4)
190	0	5.7	29.3(8)	64.9(9)
185	0	5	30(1)	65(1)
180	0	0	$\alpha + \beta$	✓
$\leq 170$	Solid	0	0	✓

**Table S2**

Refined lattice parameters of DMSO- $d_6$ ·3D<sub>2</sub>O as a function of temperature from each of the samples in which the phase occurred.

T (K)	<i>a</i> (Å)	<i>b</i> (Å)	<i>c</i> (Å)	$\beta$ (°)	V (Å <sup>3</sup> )
<b>Sample-1</b>					
195	10.26711(4)	7.01160(3)	10.06980(4)	101.5042(3)	710.351(3)
185	10.25391(8)	7.00768(6)	10.06027(7)	101.430(1)	708.556(6)
175	10.24097(9)	7.00462(6)	10.05061(9)	101.356(1)	706.856(7)
165	10.22819(10)	7.00186(7)	10.04107(10)	101.284(1)	705.204(8)
155	10.21627(12)	6.99876(8)	10.03219(11)	101.217(1)	703.612(9)
145	10.20524(13)	6.99604(8)	10.02308(13)	101.152(1)	702.098(10)
135	10.19430(14)	6.99350(8)	10.01434(14)	101.082(1)	700.648(10)
125	10.18299(15)	6.99144(9)	10.00594(15)	101.012(1)	699.245(11)
115	10.17241(16)	6.98954(9)	9.99742(15)	100.936(1)	697.914(11)
105	10.16206(16)	6.98768(9)	9.98983(16)	100.870(1)	696.643(11)
95	10.15221(18)	6.98597(10)	9.98255(17)	100.801(1)	695.449(12)
85	10.14279(17)	6.98432(9)	9.97583(15)	100.738(1)	694.317(11)
75	10.13444(16)	6.98270(9)	9.97008(15)	100.681(1)	693.316(11)
65	10.12622(16)	6.98134(9)	9.96459(15)	100.630(1)	692.353(11)
55	10.11897(16)	6.98005(9)	9.95964(14)	100.580(1)	691.500(11)
45	10.11204(16)	6.97898(9)	9.95579(15)	100.535(1)	690.754(11)
35	10.10583(17)	6.97801(9)	9.95274(15)	100.501(1)	690.099(12)
30	10.10322(16)	6.97766(8)	9.95128(14)	100.482(1)	689.826(11)
25	10.10137(17)	6.97740(9)	9.95053(15)	100.476(1)	689.635(11)
20	10.09961(16)	6.97713(8)	9.94969(15)	100.462(1)	689.461(11)
15	10.09884(16)	6.97689(8)	9.94925(14)	100.460(1)	689.358(11)
10	10.09847(9)	6.97683(5)	9.94931(9)	100.458(1)	689.336(6)
<b>Sample-2</b>					
205	10.28024(4)	7.01445(3)	10.08060(4)	101.5836(4)	712.109(4)
200	10.27463(5)	7.01228(4)	10.07540(6)	101.5457(5)	711.230(4)
195	10.26877(7)	7.01007(6)	10.07013(7)	101.506(1)	710.328(6)
190	10.26233(8)	7.00873(6)	10.06519(8)	101.467(1)	709.496(7)
185	10.25614(9)	7.00632(7)	10.05989(9)	101.431(1)	708.543(8)
175	10.24134(5)	7.00289(4)	10.05166(6)	101.3497(5)	706.796(4)

**Table S2, continued**

T (K)	<i>a</i> (Å)	<i>b</i> (Å)	<i>c</i> (Å)	$\beta$ (°)	V (Å <sup>3</sup> )
<b>Sample-3</b>					
200	10.27354(9)	7.01277(7)	10.07592(10)	101.541(1)	711.253(8)
197.5	10.27140(26)	7.01229(20)	10.07467(26)	101.517(2)	711.029(21)
<b>Sample-4 (first annealing)</b>					
202.5	10.27640(10)	7.01350(8)	10.07805(10)	101.558(1)	711.632(9)
200	10.27340(11)	7.01270(8)	10.07556(11)	101.538(1)	711.218(9)
197.5	10.26966(9)	7.01189(7)	10.07292(9)	101.517(1)	710.743(8)
195	10.26709(15)	7.01038(12)	10.07048(14)	101.494(1)	710.297(12)
<b>Sample-5</b>					
200	10.27351(13)	7.01297(10)	10.07600(13)	101.541(1)	711.277(11)
195	10.2683(5)	7.0107(4)	10.0712(5)	101.493(5)	710.46(4)

**Table S3**

Parameters obtained by fitting of a second-order Debye model to the unit-cell parameters of DMSO- $d_6$ ·3D<sub>2</sub>O between 10 and 195 K. The unit-cell edges, for dimensional reasons, are fitted as their cubes, but the ‘derived’ quantities present the results as linearized values.

	$a^3$	$b^3$	$c^3$	V
$\theta_D$ (K)	120(3)	110(7)	197(7)	139(3)
$X_0$ (cm <sup>3</sup> mol <sup>-1</sup> )	155.044(9)	51.129(2)	148.291(9)	103.786(3)
$Q$ (x10 <sup>4</sup> J cm <sup>-3</sup> )	183(3)	876(28)	200(7)	310(5)
$b$	5.5(3)	51(2)	5.0(7)	11.4(5)
Derived parameters				
$X_0$ (Å, Å <sup>3</sup> )	10.098(1)	6.9768(5)	9.950(1)	689.36(4)
$K_0/\gamma$	11.8(2)	171(5)	13.5(5)	29.9(5)
$K_0'$	12.1(5)	104(5)	11(1)	24(1)